

Technische Hochschule Nürnberg Georg Simon Ohm  
Fakultät Elektrotechnik Feinwerktechnik Informationstechnik

Studiengang Elektronische und Mechatronische Systeme  
Vertiefungsrichtung Kommunikationstechnik

Masterarbeit von  
Julian Lenhart

**Development and Validation of a GNSS-based  
Alignment Determination System for Calibration  
Targets for Satellite based Radar Systems with High  
Precision**

Wintersemester 2022/2023

Abgabedatum: 31.01.2023

Erstprüfer:	Professor Dr. Thomas Lauterbach
Zweitprüfer:	Professor Dr. Reinhard Janker
Betreuer DLR e.V.:	Dr. Jens Reimann

Hinweis: Diese Fassung der Arbeit spiegelt die Abgabeverion wieder. Es wurden keine Korrekturen im Zuge der Bewertung an dieser Arbeit vorgenommen! Keine Haftung für Fehler und Irrtümer!

Remark: This version of this thesis is turned in for evaluation at university. No corrections were made to this thesis in the course of the evaluation. No liability for mistakes and errors!

## **Abstrakt**

Die Kalibrierung von satellitengestützten Radarsystemen spielt eine entscheidende Rolle für präzise und zuverlässige Messungen. Zur Kalibrierung dieser Radarsysteme können unter anderem Winkelreflektoren als Kalibrierreferenz verwendet werden. Fehler in der Ausrichtung dieser Reflektoren führen zu Fehlern in der Kalibrierung, die es zu vermeiden gilt.

In dieser Masterarbeit wird ein Messgerät zur Bestimmung der Ausrichtung und der Position des Phasenzentrums von trihedralen und dihedralen Corner Reflektoren präsentiert. Das Messgerät basiert auf einem GNSS-Empfänger zur Ermittlung der Position und des Azimutwinkels und eines zwei Achsen-Neigungsmesser zur Bestimmung des Elevationswinkels und des Rollwinkels. Mit Hilfe des Real Time Kinematik (RTK) Verfahrens kann die Position des Phasenzentrums der Corner Reflektoren mit einer Genauigkeit im Bereich von einigen Millimetern bestimmt werden. Zur Bestimmung des Azimuts wird eine Konfiguration aus zwei Antennen verwendet sowie das Inklinometer zur Bestimmung der Elevation und des Rollwinkels mit einer Messungenauigkeit von weniger als 0,5 Grad. Das Konzept und die Implementierung des Messgeräts werden näher erläutert. Mögliche Fehlereinflüsse und verschiedene Evaluationsmethoden werden betrachtet und analysiert und eine passende Strategie zur Validierung des Messgeräts wird ermittelt. Die Ergebnisse dieser Validierung werden präsentiert und anschließend diskutiert.

## **Abstract**

The calibration of satellite based radar systems is a crucial part for precise and reliable measurements. For the calibration, corner reflectors are often used as reference. Misalignments of these corner reflectors result in errors in the calibration.

In this master thesis, a measurement instrument for the determination of the alignment and position of the phase center of trihedral and dihedral corner reflectors is presented. The device uses a GNSS receiver for the determination of the position and the azimuth and a dual axis inclinometer for the elevation and the roll angle of the corner reflector. An accuracy of a few millimeters can be reached for the position of the phase center of the corner reflectors using GNSS real time kinematic (RTK) positioning method. The device uses a GNSS multiantenna configuration for the determination of the azimuth and the dual axis inclinometer for the determination of the elevation and roll angle with an uncertainty below 0.5 degrees. The concept of the developed device is described. Error influences and different evaluation methods are analyzed, and a suitable verification strategy is selected. Finally, the results of the validation are presented and discussed.

# Contents

<b>List of Figures</b>	<b>iii</b>
<b>List of Tables</b>	<b>v</b>
<b>List of Abbreviations</b>	<b>vi</b>
<b>List of Symbols</b>	<b>vii</b>
<b>1 Introduction</b>	<b>1</b>
1.1 Introduction to the Microwave and Radar Institute of German Aerospace Center (DLR) . . . . .	1
1.2 Motivation and Objective of the Thesis . . . . .	1
1.3 Structure of the Thesis . . . . .	2
<b>2 Theoretical Fundamentals</b>	<b>3</b>
2.1 Synthetic Aperture Radar (SAR) . . . . .	3
2.1.1 Functionality of Synthetic Aperture Radar (SAR) . . . . .	4
2.1.2 Corner Reflectors for Calibration of SAR Satellites . . . . .	7
2.2 Coordinate Systems and Angle Definitions . . . . .	11
2.2.1 Worlds Geodetic System 1984 (WGS 84) and its Reference Coordinate Systems . . . . .	11
2.2.2 East-North-Up (ENU) Coordinate System . . . . .	15
2.2.3 Euler Angles and Coordinate Transformations . . . . .	16
2.3 GNSS Systems . . . . .	18
2.3.1 Structure and Functionality of a GNSS System . . . . .	18
2.3.2 RTK and Multi Antenna Sensing for Attitude and Position Determination . . . . .	21
<b>3 State of the Art</b>	<b>24</b>
<b>4 Developement of the Alignment Measurement Instrument</b>	<b>26</b>
4.1 Concept of the Instrument . . . . .	26
4.1.1 Positioning of the GNSS Antennas . . . . .	27
4.1.2 Hardware Concept . . . . .	29
4.1.3 Software Concept . . . . .	31
4.2 Hardware Implementation of the Concept . . . . .	39
<b>5 Validation of the Alignment Measurement Tool</b>	<b>42</b>
5.1 Instrument Error Estimation . . . . .	42
5.2 Strategy of Validation . . . . .	45

5.3	Results of the Validation . . . . .	47
5.3.1	Results of Single Component Validation . . . . .	47
5.3.2	Results of Instrument Validation and Discussion of the Results . . .	61
<b>6</b>	<b>Summary and Outlook</b>	<b>70</b>
	<b>References</b>	<b>72</b>
<b>A</b>	<b>Appendix</b>	<b>77</b>



# List of Figures

1	Block diagram of a monostatic SAR-system [1] . . . . .	4
2	Illustration of SAR imaging [2] . . . . .	6
3	Geometry of a triangle trihedral corner reflector [3]. . . . .	9
4	Radar Cross Section (RCS) pattern of a trihedral corner reflector above a perfectly conducting ground plane with a panel area of $50\lambda^2$ and at a frequency of 9.5 GHz in dependency of azimuth angle [4] . . . . .	10
5	Worlds Geodetic System 1984 (WGS84)s geodetic and cartesian WGS84 coordinate systems : (a) cartesian coordinate system [5] and (b) geodetic coordinate system [6] . . . . .	13
6	East North Up (ENU) coordinate system definition in Earth Centerd Earth Fixed (ECEF) coordinate system [6] . . . . .	15
7	Definition of roll-pitch-yaw representation for an aircraft [7]. . . . .	17
8	Position determination with three satellites (F) on a 2D plane using hyperbola [8] . . . . .	20
9	Trihedral corner reflector with antenna fixations and measurement instrument	27
10	Dihedral corner reflector with antenna fixations and instrument housing for the electronics . . . . .	28
11	Block diagram of the measurement instrument . . . . .	29
12	UML class diagram of the measurement instrument . . . . .	31
13	Corner reflector models with reference coordinate system: (a) trihedral corner reflector model and (b) dihedral corner reflector model . . . . .	34
14	Projection of phase center vector of corner reflectors baseplate . . . . .	36
15	Structure of the webserver . . . . .	38
16	Realisation of the alignment measurement instrument . . . . .	41
17	Inclinometer 1 deviation from 25°C value over temperature (a) x axis angle deviation over temperature (b) y axis angle deviation over temperature . .	48
18	Inclinometer 2 deviation from 25°C value over temperature (a) x axis angle deviation over temperature (b) y axis angle deviation over temperature . .	49
19	Simulation results for the algorithm comparing the pitch and roll angle . .	53
20	Simulation results for the algorithm comparing the pitch angle to all three coordinate planes . . . . .	56
21	Simulation results for the algorithm comparing the pitch angle of the baseplate determined with projection to the z-axis . . . . .	58
22	Reference measurement setup (a) tachymeter with GNSS receiver for position determination (b) markers on corner reflectors corners . . . . .	62
23	Deformation of the corner reflector used for the validation; corner size: 1.5 m	63
24	Measurement setup for the validation of the measurement instrument . . .	65

25	Flow chart of the receiver interface process . . . . .	77
26	Flow chart of the main program . . . . .	78

## List of Tables

2	Accuracy of the attitude angles of DCM method determined by PolaRx2 receiver [9] . . . . .	23
3	Standard deviation of inclinometer's axis angle deviation over temperature and during long and short time stability at room temperature . . . . .	50
4	Overview of uncertainties for pitch and roll angle of the selected inclinometer 1 . . . . .	51
5	Overview of optimizer error function algorithms and simulation results . .	59
6	Transformation error and antenna position and baseplate pitch angle to x-y plane deviation of the different error function algorithms in the practical test	60
7	Alignment angle comparison between both reference measurement methods	64
8	Results of the offset method's alignment measurement of the measurement instrument with noise and repeatability measure and reference bias. . . .	66
9	Results of projection method's alignment measurement of the measurement instrument with noise and repeatability measure and reference bias. . . .	66
10	Reference measurement of corner reflector's phase center in the ETRS89/DREF91 reference coordinate frame . . . . .	67
11	Results of phase center position measurement determined by the measurement instrument . . . . .	68
12	Specifications of the developed measurement instrument for corner reflector alignment . . . . .	71

# List of Abbreviations

**DLR** German Aerospace Center

**RCS** Radar Cross Section

**WGS84** Worlds Geodetic System 1984

**SAR** Synthetic Aperture Radar

**RTK** Real Time Kinematic

**GNSS** Global Navigation Satellite System

**LTE** Long Term Evolution

**RTCM** Radio Technical Commission for Maritime services

**ADC** analog to digital converter

**DEM** Digital Elevation Model

**PRI** Pulse Repetition Interval

**ECEF** Earth Centerd Earth Fixed

**ENU** East North Up

**MEO** Medium Earth Orbit

**PCV** Phase Center Variation

**ARP** Antenna Reference Point

**CDMA** Code Division Multiple Access

**FDMA** Frequency Division Multiple Access

**PRN** Pseudo-Random Number

**MEMS** Micro Electro Mechanical System

**USB** Universal Serial Bus

**NTRIP** Networked transport of Radio Technical Commission for Maritime services (RTCM) via Internet Protocol

**I2C** Inter-Intergrated Circuit

**SBF** Septentrio Binary Format

**NMEA** National Marine Electronics Association

**ASCII** American Standard Code for Information Interchange

**SNMP** Simple Network Management Protocol

**REST** Representational State Transfer

**API** Application Programming Interface

**UTC** Coordinated Universal Time  
**PVT** Position Velocity Time  
**LNA** Low Noise Amplifier  
**ITRS** International Terrestrial Reference System  
**ITRF** International Terrestrial Reference Frame  
**ETRS** European Terrestrial Reference System  
**ETRF** European Terrestrial Reference Frame

## List of Symbols

$P_E$	received power
$P_S$	emitted power
$\bar{S}_{ZE}$	power density at the receiving antenna of the radar
$A_{W_{eff}}$	effective area of an antenna
$G_S$	sender antenna gain
$G_E$	receiver antenna gain
$\sigma_r$	RCS of an object
$R_Z$	distance from the emitting radar antenna to the object to observe
$R_E$	distance from the object to observe to the receiving radar antenna
$L_{ges}$	overall loss of the transmission
$r_0$	shortest distance of approach between SAR and a point on earth
$v$	velocity
$c$	speed of light
$x_0$	x-coordinate of observed point by SAR
$t$	time
$\Delta h$	Height difference between the ground line and the point observed by SAR
$H$	Height of SAR satellite above the ground
$\Theta_a$	antenna beam width
$L_{sa}$	Length of synthetic aperture
$\lambda_r$	operational wavelength of radar system
$d_a$	length of real SAR antenna
$t_{PRI}$	time between two consecutive SAR pulses
$\sigma_{triangle,peak}$	peak RCS of a trihedral corner reflector
$\sigma_{dihedral,peak}$	peak RCS of a dihedral corner reflector
$a$	length of trihedral / dihedral reflector's edge
$b$	width of a dihedral corner reflector plate
$\lambda$	wavelength

$\Psi_0$	angle between the bore-sight and the baseplate of a corner reflector
$\Theta$	azimuth angle
$\Psi$	elevation angle
$\Phi_{lat}$	latitude
$\lambda_{lon}$	longitude
$h$	height over ellipsoid
$f_{lat}$	flattening of ellipsoid
$a_{ell}$	semi-major axis of ellipsoid
$b_{ell}$	semi-minor axis of ellipsoid
$e$	eccentricity of the ellipsoid
$R_{ECEF2ENU}$	transformation matrix from ECEF coordinate system to ENU frame
$\Delta X_{ECEF}$	x difference between P and point to transform into ECEF coordinates
$\Delta Y_{ECEF}$	y difference between P and point to transform into ECEF coordinates
$\Delta Z_{ECEF}$	z difference between P and point to transform into ECEF coordinates
$\Delta X_{ENU}$	x difference of point in ENU coordinates to origin of ENU frame P
$\Delta Y_{ENU}$	y difference of point in ENU coordinates to origin of ENU frame P
$\Delta Z_{ENU}$	z difference of point in ENU coordinates to origin of ENU frame P
$\Psi_r$	roll angle
$\Theta_p$	pitch angle
$\phi_y$	yaw angle
$R_x(\Psi_r)$	Rotation matrix for the roll angle
$R_y(\Theta_p)$	Rotation matrix for the pitch angle
$R_z(\phi_y)$	Rotation matrix for the yaw angle
$Trans_x(d)$	Translation matrix for translation in x coordinate by d
$x_{aux}, y_{aux}, z_{aux}$	coordinates of the auxiliary antenna with respect to the main antenna
$l_{baseline}$	baseline length of the corner reflector
$l_{inner}$	inner edge length of the trihedral corner reflector (equivalent to $a$ )
$l_{fixation}$	length of the GNSS antenna's fixations
$l_{plate}$	length of dihedral corner reflector's plate
$\alpha$	elevation angle of corner reflector's baseplate
$\vec{bp}$	vector of reflector's baseplate pointing from the phase center to the edge
$e_e, e_n, e_u$	unit vectors of the ENU coordinate frame
$\vec{P}_{up}$	Projected vector onto the up coordinate axis
$\vec{P}_{north}$	Projected vector onto the east-north plane
$\vec{n}$	normal vector pointing in the direction of the bore sight
$n_{east}$	east coordinate of the normal vector $\vec{n}$
$n_{north}$	north coordinate of the normal vector $\vec{n}$
$n_{up}$	up coordinate of the normal vector $\vec{n}$
$\sigma$	standard deviation

$\Delta pitch$	change of pitch angle
$\Delta d$	deformation of corner reflector plate
$\sigma_{sys}$	combined standard deviation for component
$\sigma_{3D}$	3D standard deviation of position
$\sigma_{hor}$	horizontal accuracy of position as $1\sigma$
$\sigma_{ver}$	vertical accuracy of position as $1\sigma$
$P_{meas}$	measured position coordinates of main and auxiliary antenna
$P_{model}$	position coordinates of main and auxiliary antenna from transformed model
$roll_{xy,ref}$	reference roll angle of baseplate to x-y plane
$roll_{xy,model}$	roll angle of baseplate to x-y plane of transformed model
$pitch_{xy,ref}$	reference pitch angle of baseplate to x-y plane
$pitch_{xy,model}$	pitch angle of baseplate to x-y plane of transformed model
$min(x)$	minimization function of optimizer
$pitch_{yz,ref}$	reference pitch angle of baseplate to y-z plane
$pitch_{yz,model}$	pitch angle of baseplate to y-z plane of transformed model
$pitch_{xz,ref}$	reference pitch angle of baseplate to x-z plane
$pitch_{xz,model}$	pitch angle of baseplate to x-z plane of transformed model
$f_i(x_{final})$	Error of optimizer with final parameters $x_{final}$
$err_{opt}$	error of the optimizer
$x_{final}$	final parameters determined by the optimizer
$err_{angle}$	final error of the compared angles of the optimizer
$main_{err,east}$	final error of main antenna's east coordinate
$main_{err,north}$	final error of main antenna's north coordinate
$main_{err,up}$	final error of main antenna's up coordinate
$std(x)$	standard deviation of measurement series x
$mean(x)$	mean value of measurement series x
$\sigma_{ENU}$	approximated standard deviation of position in ENU frame
$T_{geo,ENU}\{x\}$	Transformation from geodetic to ENU coordinates for position x
$P_{geo}$	position in geodetic coordinates
$\sigma_{geo}$	standard deviation of position in geodetic frame
$P_{ENU}$	position in ENU coordinates

# 1 Introduction

Today radar satellites play an important role in earth observation and cartography. The radar images are used to observe and monitor climate dynamics and changes on Earth like the melting of glaciers and the polar caps. Additionally, the structure of vegetation like deforestation and canopy heights can be monitored to improve forest, fire and nature protection. Another application is the reconnaissance of areas after natural disasters like floodings and earthquakes providing an overview for rescue teams and crisis management. Potential flooding or tsunami endangered areas can be identified and the generated maps can be used for risk evaluation and risk mitigation. For geology, the radar satellites can provide information about height changes after earthquakes and volcanic activities. In case of cartography, radar satellites can provide a map of the Earth with an uniform and precise height model which can be used for navigation especially for improving the reliability of ground proximity systems and synthetic vision systems for airplanes. The satellites can be operated independent of the illumination from the sun and weather conditions like cloudiness due to radar imaging. This is an advantage over optical satellite imaging. [10], [11]

In order to provide reliable and precise data for all these applications, calibration is needed for the satellites. The DLR has established a SAR calibration centre which provides calibration services for many national and international SAR missions, like the German TerraSAR-X and TanDEM-X [10] or ESA's Sentinel-1 system.

## 1.1 Introduction to the Microwave and Radar Institute of DLR

The Institute of Microwave and Radar of DLR researches and develops SAR based systems and applications for ground, airborne and satellite remote sensing [12]. This thesis is written in the 'Satellite SAR Systems' department in the calibration group. The department develops satellite based SAR systems and takes care of the operation and the calibration of the satellites. Tasks of the department contain, among others, the SAR systems engineering, analysis of SAR system performances, calibration, and mission planning. [13] The calibration group focuses on the development of reference targets such as transponders and calibration methods and techniques for radar systems. The group provides various calibration services like a calibration field for international SAR missions and analysis tools. [13]

## 1.2 Motivation and Objective of the Thesis

As reference targets for the calibration of DLR's radar satellites, corner reflectors are used among others. They reflect the radar signal back to the radar satellite. The reflector must be aligned towards the direction where the radar satellite is located during



the overflight to provide a perfect and precise calibration. So far, the alignment of the reflector is determined manually with an inclinometer for the elevation angle and with a magnet compass for the azimuth angle. As reference for the determination of the azimuth angle the geodetic north pole must be used. With a compass the azimuth angle is falsified by the difference in the positions of the magnetic and the geodetic north pole as well as by the influence of metallic objects near the compass. Due to these effects, the accuracy of the angle determination is decreased. Additionally, there is a loss in accuracy due to the reading accuracy of about  $0.5^\circ$  from the scales of the measurement equipment. Furthermore, the azimuth and the elevation angle measured with the compass and the inclinometer are not equal to the bore sight alignment of the corner reflector. Due to this, the setpoint values for the compass and inclinometer must be calculated in advance. The whole alignment determination process shall be simplified, and the accuracy of the attitude angles shall be improved.

In order to improve the accuracy of the alignment and to ease the alignment process, a mobile, light weighted, easy to mount measurement instrument with low power consumption shall be conceptualized, developed, and build. The instrument shall be validated in order to determine the accuracy of the device, which is an essential property for calibration tasks and the traceability of uncertainties. The base of the instrument shall be a Global Navigation Satellite System (GNSS) receiver and an inclinometer. Inexpensive, geodetic-grade GNSS receivers became only recently available to enable these kind of applications. These sensors shall be used for the determination of the attitude / alignment angles and the position of the corner reflectors reflection point, e.g. the phase center. The attitude shall be easy readable on a display or on a mobile phone via a Wi-Fi network. The development of the mounting fixation for the instrument and the antennas is not part of the thesis but shall be discussed and conceptualized together with the mechanics team. The instrument shall be developed primarily for trihedral corner reflectors considering in the design the extension for the usage of the instrument with dihedral corner reflectors. Only available components with short lead times shall be selected and ordered in the early stage of the project to avoid long lead times.

### **1.3 Structure of the Thesis**

Firstly, the theoretical background knowledge is given in order to provide a better understanding of the content of this thesis. The context and differences with other state-of-the-art projects using GNSS for the determination of the attitude and precise positioning is shown. After this, the requirements for the instrument and the derived concept and implementation is explained. The validation strategy with its error estimation is described and results of the verification of the measurement instrument are presented and discussed. Finally, a summary is provided, and an outlook is given.

## 2 Theoretical Fundamentals

The chapter 'Theoretical Fundamentals' contains the basic knowledge which is needed to understand the thesis' content and the larger background of the thesis. At first, the principles and basic functionality of SAR is explained. The radar satellites of DLR, TerraSAR-X and TanDEM-X, use SAR technique for imaging and observation of the earth. Also the structure and functionality of corner reflectors which are used for the calibration of DLR's SAR satellites is presented.

Afterwards, an overview of the different coordinate systems is given that are used throughout this thesis and the algorithms for the transformation between these coordinate systems are shown. Mainly the WGS84 ellipsoid for the approximation of Earth's geoid and the local East-North-Up coordinate system are presented. The Euler angles convention is explained and the rotational and translation matrixes are provided for transformation between local coordinate systems.

Last but not least, the structure and functionality of a GNSS system is described. GNSS systems are used to extract the position of the corner reflector as well as for the determination of the heading of the corner reflector. Therefore, the Real Time Kinematic (RTK) positioning mode needed for precise position determination and multi antenna configuration needed for the determination of the heading from two antenna positions are explained.

### 2.1 Synthetic Aperture Radar (SAR)

Synthetic Aperture Radar (SAR) is a imaging radar for airborne or spaceborne systems that often uses pulsed radar signals. The vehicle where the SAR is mounted is constantly moving forward in the along track or azimuth direction and the radar is mounted in a side looking configuration on the vehicle. The pulses sent by the radar are backscattered from the observable object and received again by the radar. If the backscatter is received by the same antenna as the transmitting antenna, the radar is classified as monostatic radar. If the echo is received by a different antenna than the transmitting antenna, the radar is called bistatic radar for two antennas or multistatic radar for more than two antennas. [2], [1]

DLR's SAR satellite TerraSAR-X is a monostatic SAR system and can form together with the TanDEM-X satellite a bistatic SAR system due to a formation flight of the two satellites in a helix shaped orbit and the usage of both satellite's antennas for reception of each other's radar pulses. This configuration allows the generation of 3D radar images due to the reception of the same radar signal at two different places with different roundtrip times and to form an interferometer. This allows for 3D imaging comparable to seeing with two eyes. With this radar system it is possible to generate a high resolution height model of the Earth, also known as Digital Elevation Model (DEM). [11]

Due to the use of radar signals, no external illumination from the sun is needed for

imaging. Therefore, the SAR can be used even at night which provides a huge advantage over optical imaging systems. SAR is operated in the microwave bands which allows the penetration of clouds, soil and other substances. With different polarization of the electromagnetic radar pulse and reception of different polarizations of the radiated pulse, the physical and electrical characteristics like roughness and geometry of the observed objects or surfaces can be determined. [14], [2]

In the following chapter, a basic knowledge of the functionality of SAR is provided. For a more detailed introduction to SAR it shall be referred to the sources [2], [14] and, [15].

### 2.1.1 Functionality of SAR

A SAR system often uses a pulse generator to generate radar pulses which are then amplified and converted to the transmitting frequency by the sender. A circulator prevents that signals from the sender are able to traverse to the receiver and that received signals from the antenna traverse into the sender. The received echoes are filtered and amplified by the receiver. Afterwards the signals are demodulated and digitalized with an analog to digital converter (ADC). The data is then processed by a SAR processor which creates a SAR image from the raw data. The whole radar system is controlled and monitored by a radar control unit. [1]

This structure of a SAR system can be seen in the block diagram in figure 1.

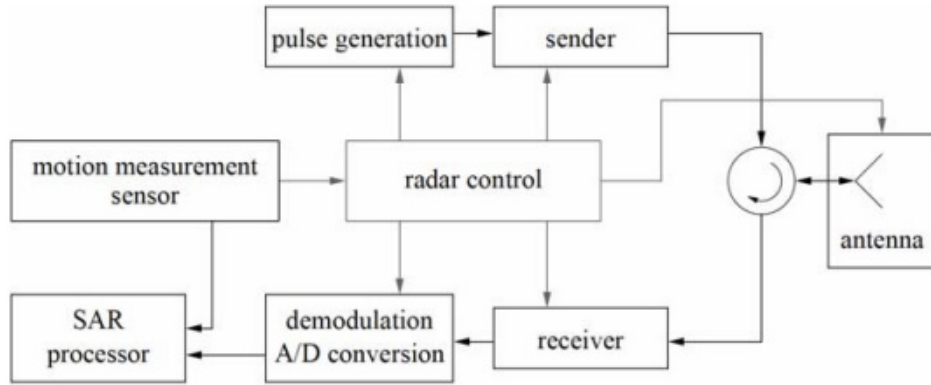


Figure 1: Block diagram of a monostatic SAR-system [1]

The received power of the transmitted pulse in dependency of the object where the radar signal is reflected can be explained with the general radar equation from [16]:

$$P_E = \bar{S}_{ZE} A_{W_{eff}} = \frac{P_S G_S G_E \lambda_r^2 \sigma_r}{(4\pi)^3 R_Z^2 R_E^2 L_{ges}} \quad (1)$$

with  $\bar{S}_{ZE}$  and  $A_{W_{eff}}$  defined as:

$$\bar{S}_{ZE} = \frac{P_S G_S \sigma_r}{(4\pi)^2 R_Z^2 R_E^2 L_{ges}}; \quad A_{W_{eff}} = \frac{G_E \lambda_r^2}{4\pi} \quad (2)$$

As can be seen in equation (1), the received power by the radar can be determined by multiplying the reflected power density at the receiving antenna  $\bar{S}_{ZE}$  with the radar antenna's effective area  $A_{W_{eff}}$  [16]. The power density at the receiving antenna is determined by the transmission power  $P_S$ , the sender antenna gain  $G_S$ , the radar cross section (RCS)  $\sigma_r$  of the object where the radar pulse is reflected, the distance from the transmitting antenna to the object  $R_Z$ , the distance from the object to the receiving antenna  $R_E$  and the overall loss of the transmission  $L_{ges}$  [16]. The RCS is a measure for the ability to reflect incident power density from a radar on an effective area back with an aperture gain [3]. For a monostatic radar system, the distances  $R_Z$  and  $R_E$  are identical. The overall loss is the sum of the loss in the radar system, the fluctuations losses, and the atmospherical losses. The system loss is the loss generated inside the radar sender and receiver by attenuation in cables or in the signal processing. Fluctuation losses are variations in the amplitude of the echoes generated by variations in the RCS of the observed object due to the overlay of different backscatter components which changes with the movement of the object. The atmospherical losses are the combination of the free field attenuation of the transmission and the additional attenuation due to gases and weather conditions like rain or fog. [16] Many SAR systems operate in the microwave band, especially in the Ka-band (40 GHz - 25 GHz), Ku-band (17.6 GHz - 12 GHz), X-band (12 GHz - 7.5 GHz), C-band (7.5 GHz - 3.75 GHz), S-band (3.75 GHz - 2 GHz), L-band (2 GHz - 1 GHz) and P-band (0.5 GHz - 0.25 GHz). The higher the frequency, the lower, in general, is the penetration in media. By coherently combining several receive echoes, a virtual antenna can be formed which can be much longer than the original antenna. Due to this effect, the radar has a larger virtual aperture than the physical length of the radar antenna. [2]

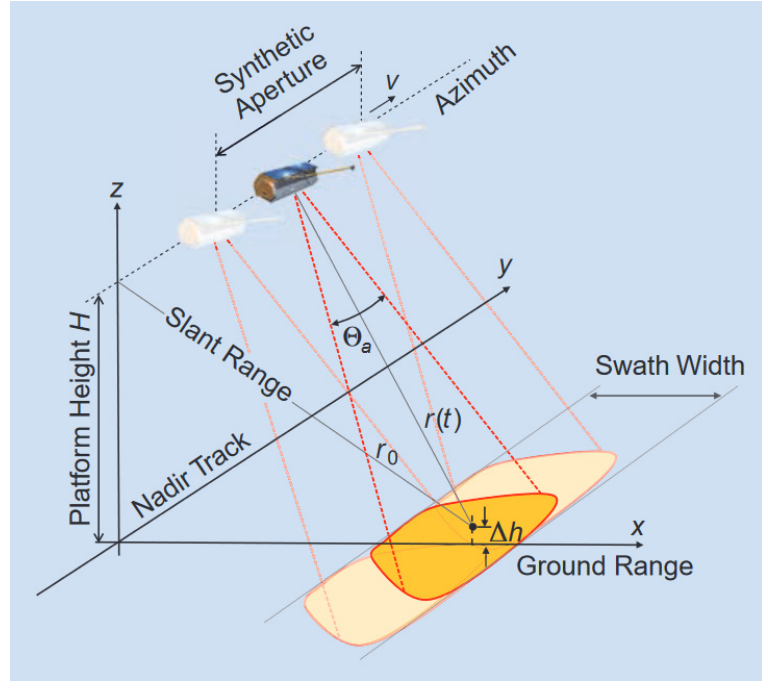


Figure 2: Illustration of SAR imaging [2]

It can be seen in figure 2 that the radar beam covers a 2D area. This illuminated area is defined by the moving direction of the satellite, which is also known as the azimuth direction, and the direction orthogonal to the azimuth direction which is called the slant range direction [2]. The emitted pulses' bandwidth determines the range resolution with an inverse proportionality. The azimuth resolution of the SAR is determined by the length of the synthetic aperture, which can be approximated by the antenna beam width  $\Theta_a$  which is calculated by dividing the wavelength of the radar signal  $\lambda_r$  through the length of the actual radar antenna  $d_a$ . [15], [2]

The slant range  $r_0$  is the shortest distance between the satellite and the point to observe and can be calculated with the following equation from [2] with  $H$  as the height of the satellite above the ground,  $\Delta h$  as the height difference of the observed point and the ground and  $x_0$  as the x coordinate of the observed point:

$$r_0 = \sqrt{(H + \Delta h)^2 + x_0^2} \quad (3)$$

With the knowledge of the slant range, the distance between the observed point and the SAR can be calculated at any time during the overflight of the satellite with the equation from [2]:

$$r(t) \approx \sqrt{r_0^2 + (vt)^2} \quad (4)$$

The length of the synthetic aperture can be approximated from the beam width and the slant range by the following equation from [2]:

$$L_{sa} \approx \Theta_a r_0 \approx \frac{\lambda_r r_0}{d_a} \quad (5)$$

A short antenna length or a large beam width allows a longer synthetic aperture and therefore a finer azimuth resolution [2].

For the sequence of operation, radar pulses are sent by the SAR instrument in fixed intervals called the *Pulse Repetition Interval (PRI)* and the echoes from the Earth's surface are received between two pulses. The received complex value resembles the amplitude and the phase of the echo. Each complex echo sample is amplified, converted down to baseband, digitalized and stored in a 1D vector. The complex data resembles the values in the slant range direction which is indicated by the runtime of the echo from the radar instrument to the object and back. With the next pulse the satellite has moved the distance of  $v \cdot t_{PRI}$  and the sequence above is repeated. With this procedure a 2D matrix can be created with the rows representing one sample in azimuth direction and the columns one sample in the range direction.[15], [2]

Due to the complexity of the processing of a radar image from this raw data, it is not covered in this thesis. Further information on radar image processing can be found in [2]. After the processing of the radar image, the real position on the ground must be assigned for every pixel in the radar image. This process is called geocoding. For monostatic SAR systems, the 3D scenery is projected onto a 2D azimuth and range image which can cause distortions in the positions due to the viewing geometry of the radar on the scenery. Additionally, there can be shadowing of objects by larger objects in front of them so that some objects cannot be illuminated by the radar. Another effect caused by the viewing angle is that elements in the scenery can appear more stretched or more compressed than they are. These areas must be corrected by postprocessing. [2]

Another step that is performed during the processing of the radar image is the calibration of the intensity of each pixel in the image to its representative value. For this calibration the RCS normalized to the area can be used [2]. The calibration is performed internally in the instrument as well as externally with reference targets with a known RCS [2]. Corner reflectors can be used as external calibration targets. In the following chapter 2.1.2, corner reflectors and their role in the calibration of SAR satellites are discussed.

### 2.1.2 Corner Reflectors for Calibration of SAR Satellites

In order to calibrate radar systems and therefore radar satellites like DLR's TerraSAR-X and TanDEM-X, targets with a known RCS as reference can be used. The RCS of an target can be influenced by surrounding objects such as trees or buildings. Therefore, the

assumption for the following calculations and DLR's reference targets is made that the targets are placed in free space without the influence of other objects. The RCS value is often provided in  $m^2$  or  $dBm^2$ . [3]

The quality of the external calibration is influenced by the following characteristics of a calibration target which are defined by [4]:

- The RCS must be much higher than the RCS of the environment around the target.
- A wide RCS pattern allows a better coherence at certain misalignments of the targets.
- A small physical target size allows a better handling of the target in the field.
- A stable RCS allows a better stability and coherence of the target.
- An insensitive RCS to the environment allows a better stability and coherence as well.

As targets for the calibration and testing of monostatic radar systems, canonical reflectors such as trihedral corner reflectors are widely used due to their high RCS, a wide RCS pattern and, resulting from this, the insensitivity to misalignments [17], [3]. Additionally, the corner reflectors can be used for observing displacements of engineered buildings such as dams or bridges [17]. Triangular trihedral corner reflectors consists of three right triangular shaped plates that are mounted orthogonal to each other with an inner edge length of  $a$ . This length must be large in comparison to the radar signals wavelength. The corner reflector has a direction of maximum RCS which is called the bore sight and is located at an elevation angle of  $\Psi_0 = \arctan\left(\frac{1}{\sqrt{2}}\right)$  ( $\approx 35, 26^\circ$ ) from each of the triangular shaped plates. [3]

The outline of the corner reflector consists of edges and corners which are referred hereinafter as vertices. The plate on the bottom can be called baseplate of the corner reflector. In figure 3, the geometry of a triangle trihedral corner reflector is shown.

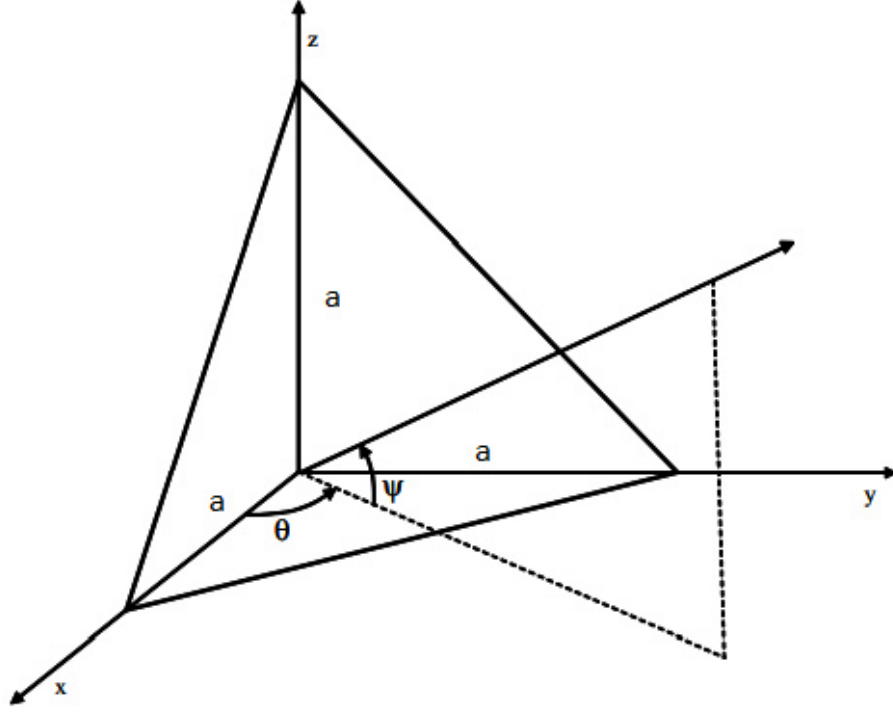


Figure 3: Geometry of a triangle trihedral corner reflector [3].

The peak RCS in the bore sight of the trihedral reflector can be calculated from the geometry of the corner reflector with the following equation from [3]:

$$\sigma_{triangle,peak} = \frac{4\pi a^4}{3\lambda^2} \quad (6)$$

It can be seen from equation (6) that for long wavelengths (low frequencies in the L- and P-band) the inner edge length  $a$  must be increased to reach a high RCS. Due to this effect, the physical size of the corner reflector increases. Deformation due to bending of the corner reflectors plates due to the increased size results in a decrease of RCS. [4]

Also deviations in the alignment of the bore sight of the reflector to the radar's line-of-sight results in a decrease of the RCS and therefore in an error in the calibrated value [3], [17].

The RCS in dependency from the elevation angle  $\Psi$  and the azimuth angle  $\Theta$  can be calculated with the following equation (7) from [3]:

$$\sigma_{triangle}(\Theta, \Psi) = \begin{cases} \frac{4\pi}{\lambda^2} a^4 \left( \frac{4c_1 c_2}{c_1 + c_2 + c_3} \right)^2 & \text{for } c_1 + c_2 \leq c_3 \\ \frac{4\pi}{\lambda^2} a^4 \left( c_1 + c_2 + c_3 - \frac{2}{c_1 + c_2 + c_3} \right)^2 & \text{for } c_1 + c_2 \geq c_3 \end{cases} \quad (7)$$

with  $c_1$ ,  $c_2$  and  $c_3$  defined as



$$c_1 = \sin \Psi \quad c_2 = \cos \Psi \sin \Theta \quad c_3 = \cos \Psi \cos \Theta \quad (8)$$

The deviation of the RCS due to misalignment of a trihedral corner reflector above a perfectly conducting ground plane with a panel area of  $50\lambda^2$  and at a frequency of 9.5 GHz is displayed in dependency of the azimuth angle in figure 4 [4].

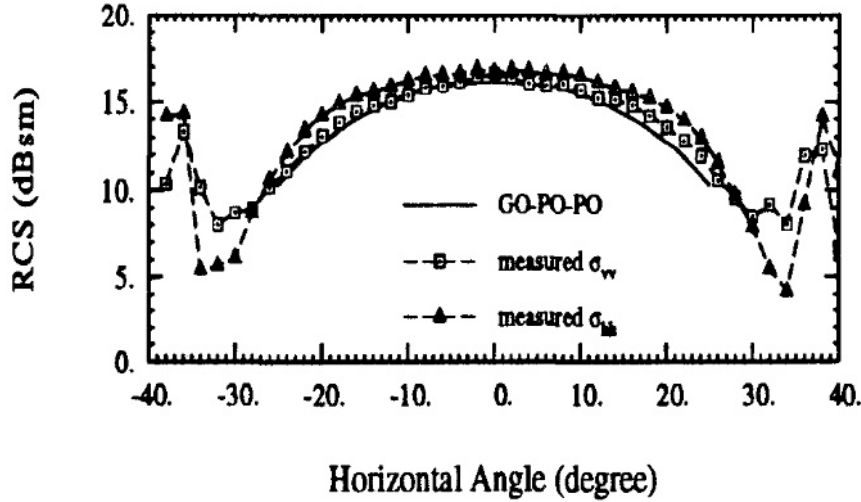


Figure 4: RCS pattern of a trihedral corner reflector above a perfectly conducting ground plane with a panel area of  $50\lambda^2$  and at a frequency of 9.5 GHz in dependency of azimuth angle [4]

In figure 4 the wide RCS pattern and the insensitivity to misalignment can be seen. [17] However, even small misalignments result in errors in the calibration. In order to achieve an accurate calibration for the SAR systems a precise alignment measurement must be provided.

SAR also measures the time delay between the transmission of the pulse and the reception of the echo from the corner reflector. If the distance between the satellite and the phase center of the corner reflector is known, the time delay can be calculated and can be compared with the measured time delay in order to identify and calibrate any deviations caused by errors. The position of a corner reflector and its geometric phase center can be determined with an accuracy in the range of millimeters due to the defined echo from the reflector. [18]

Another corner reflector type that can be used for the calibration of polarimetric radar systems is the dihedral corner reflector [19]. Typically, dihedral corner reflectors consist of two rectangular plates with an angle of about  $90^\circ$  between each other [19]. The dihedral corner reflector provides a very narrow beamwidth in the elevation plane [17]. In this thesis, only orthogonal dihedral corner reflectors are observed which resemble typical

objects like wall to ground or ship to sea surface observed with SAR systems [19]. The peak RCS of a dihedral reflector can be calculated from the length  $a$  and the width  $b$  of one of the two plates with the following equation from [16]:

$$\sigma_{dihedral,peak} = 8\pi\left(\frac{a b}{\lambda}\right)^2 \quad (9)$$

## 2.2 Coordinate Systems and Angle Definitions

In this section, the different coordinate systems used for the specification of the position and the alignment are presented and angle definitions for the alignment are provided. The World Geodetic System (WGS) Earth ellipsoid and its reference coordinate systems is used for the position definition of the alignment measurement instrument as well as the ENU coordinate system is used for the attitude angles definition. Finally the transformations are explained for the transformation between the used coordinate systems.

### 2.2.1 World's Geodetic System 1984 (WGS 84) and its Reference Coordinate Systems

The World's Geodetic System 1984 (WGS84) is the most widely used convention to approximate Earth's geoid with an ellipsoid and to provide position definitions on Earth [5]. The WGS84 geodetic datum was introduced by the US defense mapping agency (DMA) in 1984 and is also used as reference for GPS [5]. The semi-major axis  $a_{ell}$  of the ellipsoid is defined in the WGS84 Earth's model with 6378137 meters and the semi-minor axis  $b_{ell}$  with 6356752 meters. The Earth rotates around the semi-minor axis. [6]

From the semi-axis of the ellipsoid the flattening  $f_{lat}$  (0.00335281 for WGS84) and the eccentricity  $e$  (0.08181919 for WGS84) as parameters for the description of the ellipsoid can be derived with the following equations from [6].

$$f_{lat} = \frac{(a_{ell} - b_{ell})}{a_{ell}} \quad (10)$$

$$e^2 = \frac{(a_{ell}^2 - b_{ell}^2)}{a_{ell}^2} = 2f_{lat} - f_{lat}^2 \quad (11)$$

In the WGS84 ellipsoid different reference frames like International Terrestrial Reference Frame (ITRF) (global reference frame) and European Terrestrial Reference Frame (ETRF) (european reference frame) can be defined in which the position on the ellipsoid can be given. The WGS84 is based on the International Terrestrial Reference System (ITRS) with the ITRF reference frames. Therefore, the position deviations between the WGS84 and the ITRF are quite small (0.1 m). Due to the movement of the European plate of 0.025 m per year with respect to the ITRS, the coordinates in the ITRF are

timevariant for positions in Europe. In order to provide stable coordinates for positions in Europe, the European Terrestrial Reference System (ETRS) with the ETRF reference frames is introduced which frame moves with the movement of the Eurasian plate. [20] The ITRF and ETRF reference frames are described in more detail in [20].

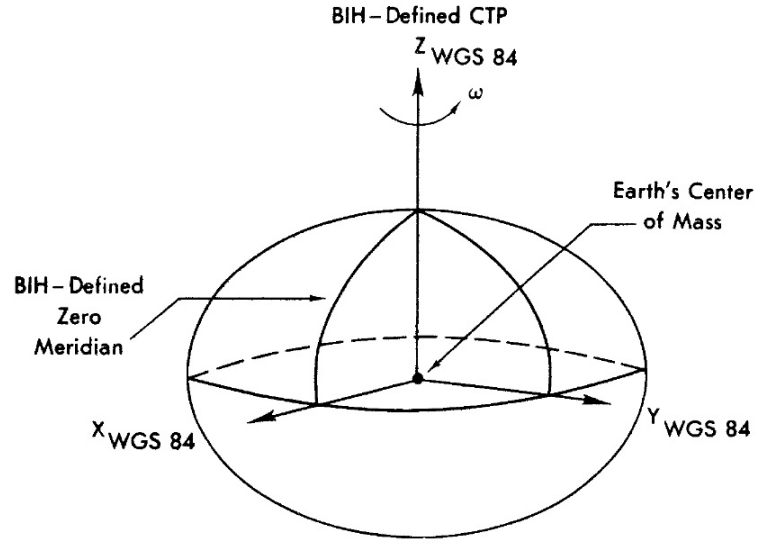
The origin of the coordinate systems is Earth's gravitational center of mass [5]. A position in these ECEF coordinate systems can be described in cartesian coordinates and in geodetic coordinates [21].

In the cartesian coordinate system, the Z-axis resembles the rotation axis of the Earth and points from the center of mass to the north pole. The X-axis is defined on the equatorial plane and points from the center of mass to the prime meridian defined by the Bureau International de l'Heure (BIH). The Y-axis is defined by the right-handed coordinate system formed by the X and Z-axis. [5], [6]

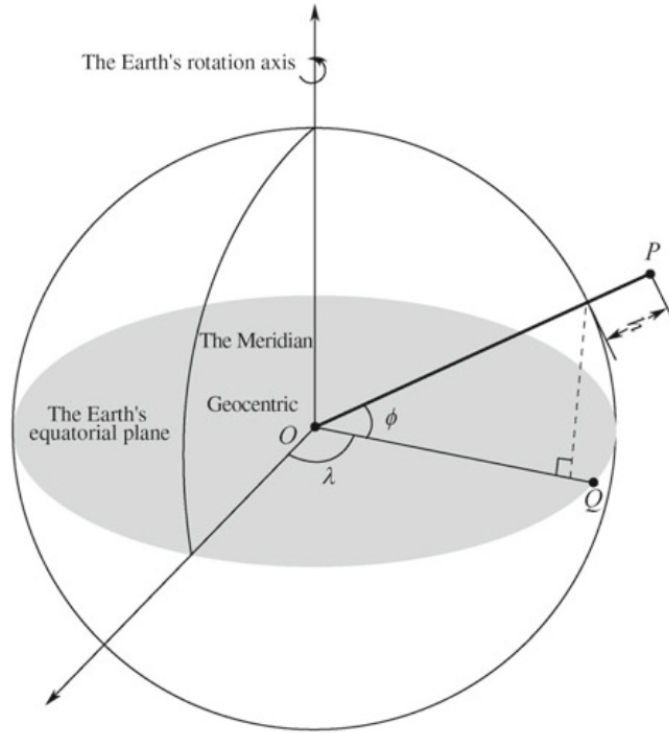
This coordinate system is displayed in figure 5 (a).

Another representation of a position on Earth's geoid in the WGS84 model are geodetic coordinates which form a polar coordinate system. A position on Earth's surface P can be expressed in the geodetic system by the latitude, longitude and height over the WGS84 ellipsoid. The latitude  $\Phi_{lat}$  is the angle between the equatorial plane and the normal vector on Earth's surface at point P from the Earth's center of mass in the range from  $-90^\circ$  (south pole) to  $+90^\circ$  (north pole). The longitude  $\lambda_{lon}$  is the angle between the projected point vector P on the equatorial plane and the zero meridian in the range from  $-180^\circ$  to  $+180^\circ$ . The height  $h$  is the height difference between point P and the projected point P' on the ellipsoid. [6]

The described geodetic coordinate system definition can be seen in figure 5 (b).



(a)



(b)

Figure 5: WGS84s geodetic and cartesian WGS84 coordinate systems :

(a) cartesian coordinate system [5] and

(b) geodetic coordinate system [6]

The geodetic coordinates can be converted to the cartesian coordinate system with the following equations from [6]:

$$x = (R_N + h) \cos(\Phi_{lat}) \cos(\lambda_{lon}) \quad (12)$$

$$y = (R_N + h) \cos(\Phi_{lat}) \sin(\lambda_{lon}) \quad (13)$$

$$z = [R_N (1 - e^2) + h] \sin(\Phi_{lat}) \quad (14)$$

with  $R_N$  as

$$R_N = \frac{a_{ell}}{\sqrt{1 - e^2 \sin^2(\Phi_{lat})}} \quad (15)$$

The conversion from the ECEF coordinates back to the geodetic coordinate system is difficult to solve with an analytical method in a practical application. Therefore, the conversion must be done with an iterative algorithm. The iterator parameters shall be initialized with the following values according to [6]:

$$h = 0; \quad R_N = a_{ell} \quad (16)$$

$$p = \sqrt{x^2 + y^2} \quad (17)$$

The following equations from [6] shall be iterated until the solution for  $\Phi_{lat}$  converges:

$$\sin(\Phi_{lat}) = \frac{z}{(1 - e^2) R_N + h} \quad (18)$$

$$\Phi_{lat} = \arctan\left(\frac{z + e^2 R_N \sin(\Phi_{lat})}{p}\right) \quad (19)$$

$$R_N = \frac{a}{\sqrt{1 - e^2 \sin^2(\Phi_{lat})}} \quad (20)$$

$$h = \frac{p}{\cos(\Phi_{lat})} - R_N \quad (21)$$

In practice it can be seen that the latitude  $\Phi_{lat}$  in equation (19) converges much faster than the latitude in equation (18) and that an accuracy of the latitude in the range of centimeters can be reached after only five iterations [6].

The longitude  $\lambda_{lon}$  does not need to be determined iteratively, but can be calculated accurately from the coordinates  $x$  and  $y$  with the following equation from [22]:

$$\lambda_{lon} = 2 \arctan\left(\frac{p-x}{y}\right) \quad (22)$$

### 2.2.2 East-North-Up (ENU) Coordinate System

The ENU coordinate system is a local tangent plane coordinate system with a point P on Earth's surface as the origin of the coordinate system. It is a right handed euclidean coordinate system with the X-axis  $X_{ENU}$  pointing in the geodetic east direction, the Y-axis  $Y_{ENU}$  pointing to the geodetic North pole and the Z-axis  $Z_{ENU}$  resembles the normal vector on the tangent plane on the Earth's geoid pointing away from the surface of the earth. [23], [6]

In figure 6 the definition of the ENU coordinate system in the ECEF coordinate system is displayed:

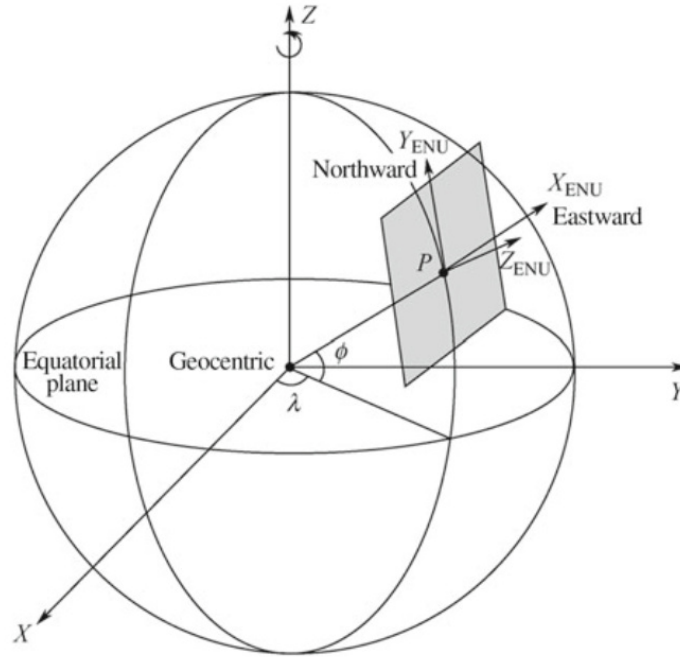


Figure 6: ENU coordinate system definition in ECEF coordinate system [6]

The coordinates of the ECEF cartesian coordinate system can be transformed to the ENU frame by multiplying with the matrix (23) from [6]. The latitude  $\Phi_{lat}$  and the longitude  $\lambda_{lon}$  are the geodetic coordinates of the point P which is the origin of the local ENU coordinate system (see figure 6). The coordinates  $\Delta X_{ECEF}$ ,  $\Delta Y_{ECEF}$  and  $\Delta Z_{ECEF}$  resembles the vector between the point that shall be transformed to the ENU system and the origin of the ENU coordinate system, point P. [8]

$$R_{ECEF2ENU} = \begin{pmatrix} -\sin(\lambda_{lon}) & \cos(\lambda_{lon}) & 0 \\ -\cos(\lambda_{lon}) \sin(\Phi_{lat}) & -\sin(\lambda_{lon}) \sin(\Phi_{lat}) & \cos(\Phi_{lat}) \\ \cos(\lambda_{lon}) \cos(\Phi_{lat}) & \sin(\lambda_{lon}) \cos(\Phi_{lat}) & \sin(\Phi_{lat}) \end{pmatrix} \quad (23)$$

The ENU coordinates can be calculated with the matrix from equation (23) with the following equation from [8]:

$$\begin{pmatrix} \Delta X_{ENU} \\ \Delta Y_{ENU} \\ \Delta Z_{ENU} \end{pmatrix} = R_{ECEF2ENU} \cdot \begin{pmatrix} \Delta X_{ECEF} \\ \Delta Y_{ECEF} \\ \Delta Z_{ECEF} \end{pmatrix} \quad (24)$$

The transformation from the ENU coordinate system back to the ECEF coordinate system can be performed by multiplying with the transposed matrix [8]:

$$\begin{pmatrix} \Delta X_{ECEF} \\ \Delta Y_{ECEF} \\ \Delta Z_{ECEF} \end{pmatrix} = R_{ECEF2ENU}^T \cdot \begin{pmatrix} \Delta X_{ENU} \\ \Delta Y_{ENU} \\ \Delta Z_{ENU} \end{pmatrix} \quad (25)$$

### 2.2.3 Euler Angles and Coordinate Transformations

The Euler angles can be used to describe the orientation of an object in a three dimensional space in its reference frame. To define the attitude of an object, three successive rotations must be performed. For these rotations, the axis around which is rotated must be defined and the axis for the next rotation must differ from the previous axis. These axis can origin from a fixed coordinate frame or from a coordinate frame moving with each rotation. There are 12 possible rotation patterns which can be used to define rotation conventions. [7]

One of these conventions is the roll-pitch-yaw representation which describes the rotation pattern in a fixed coordinate frame with a first rotation around the x-axis by the angle roll, a second rotation around the y-axis by the angle pitch and finally a rotation around the z-axis by the angle yaw (XYZ) [7]. As example, for an aircraft, the representation is a right-handed moving coordinate system with the center of mass as origin, the x-axis pointing to the nose of the aircraft, the y-axis pointing in the direction of the right wing and the z-axis pointing down to the ground. This definition of the roll-pitch-yaw for an aircraft is shown in figure 7.

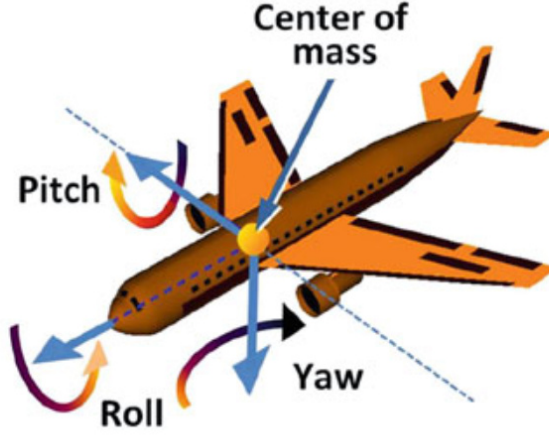


Figure 7: Definition of roll-pitch-yaw representation for an aircraft [7].

Mathematically the rotations can be expressed by a multiplication of a point with the following matrices from [7] with roll as  $\Psi_r$ , pitch as  $\Theta_p$  and yaw as  $\phi_y$  in the defined convention order.

$$R_x(\Psi_r) = \begin{pmatrix} 1 & 0 & 0 & 0 \\ 0 & \cos(\Psi_r) & -\sin(\Psi_r) & 0 \\ 0 & \sin(\Psi_r) & \cos(\Psi_r) & 0 \\ 0 & 0 & 0 & 1 \end{pmatrix} \quad (26)$$

$$R_y(\Theta_p) = \begin{pmatrix} \cos(\Theta_p) & 0 & \sin(\Theta_p) & 0 \\ 0 & 1 & 0 & 0 \\ -\sin(\Theta_p) & 0 & \cos(\Theta_p) & 0 \\ 0 & 0 & 0 & 1 \end{pmatrix} \quad (27)$$

$$R_z(\phi_y) = \begin{pmatrix} \cos(\phi_y) & -\sin(\phi_y) & 0 & 0 \\ \sin(\phi_y) & \cos(\phi_y) & 0 & 0 \\ 0 & 0 & 1 & 0 \\ 0 & 0 & 0 & 1 \end{pmatrix} \quad (28)$$

The used GNSS receiver mosaic-go from Septentrio uses the same roll-pitch-yaw coordinate frame definition as shown in figure 7. The rotations are defined as the successive rotation around the three vehicle frame axes relative to a local ENU coordinate frame which is described in chapter 2.2.2. From the x-axis pointing in the north direction, y-axis pointing in the east direction and z-axis pointing down, the following moving coordinate frame rotation order is defined by the receiver: First a rotation around the z-axis by the angle yaw. Second the new coordinate frame is rotated around the y-axis by the pitch angle. Finally, the coordinate frame generated by the second rotation is rotated around the x-axis by the roll angle. [24]



This Z'Y'X' rotation convention in a moving coordinate frame is identical to the rotation around the x, y and z-axis in a fixed coordinate frame [25].

Another important step for the transformation between different reference frames is the translation, also known as displacement [25]. The translation equals an addition of an offset to the coordinates of a point [25]. The translation of the offset  $d$  in x-axis direction can be expressed by multiplying the point that shall be transformed with the following matrix from [25].

$$Trans_x(d) = \begin{pmatrix} 1 & 0 & 0 & d \\ 0 & 1 & 0 & 0 \\ 0 & 0 & 1 & 0 \\ 0 & 0 & 0 & 1 \end{pmatrix} \quad (29)$$

## 2.3 GNSS Systems

GNSS is a generic term for global satellite positioning systems such as GPS, GLONASS, Galileo, and Beidou. These systems are used to retrieve the global three dimensional position on Earth from GNSS satellites. The position is determined by solving a geometric problem with known distances between the GNSS satellites and the user's GNSS receiver. At least four GNSS satellites with known positions are needed for the position calculation. [8]

In this section, the structure of a GNSS satellite constellation and the satellites itself is explained, an overview of the signal transmission, and information about the algorithms for retrieving the current position from this signal is provided. Afterwards, the algorithms used by the receiver in order to retrieve a precise position in the range of millimeters and the attitude in the range of a few tenths of degrees are presented.

### 2.3.1 Structure and Functionality of a GNSS System

A typical GNSS system consists out of three segments: the space segment, the control segment, also known as ground segment, and the user segment. In the space segment, the GNSS satellites are located which provide transmissions of the code and carrier phases to the users. For a precise timing of the transmissions, atomic clocks are installed on the satellites to generate an exact system clock and to provide the exact timing for the distance measurement. Navigation messages are uploaded to the satellites frequently from the control stations. [8]

Most satellites are located in the Medium Earth Orbit (MEO) in an altitude between 19 100 km (GLONASS) and 23 222 km (BeiDou). To allow global coverage and the visibility of enough satellites at any point for position determination, a constellation of satellites with different orbits is needed. The position is obtained upon time differences. Therefore,

a very precise time reference is needed onboard of the satellites which are equipped with very high stability rubidium, caesium or hydrogen atomic oscillators with a high stability of  $\Delta f/f \approx 10^{-13}$ . These oscillators drift away over time which is estimated by the ground segment. The corrections for the time drifts can be used by the receiver. The receiver uses quartz oscillators as clock sources which provide a much lower stability of  $10^{-9}$ , but are much cheaper as well. The offset between the two clocks can be reduced by using an additional satellite for time synchronization. [8]

The control segment takes care of controlling and maintaining the orbits of the satellites in the constellation as well as monitoring their status and functionality. The ephemeris of the satellites is predicted by the control station. The satellites clock drifts are determined and the GNSS time scale is maintained. Additionally, the ground segment provides updates for the navigation messages which are sent by the satellites to the receivers for position determination. [8]

The user segment consists of the GNSS receivers. They receive the signals from the satellite, determine the pseudo ranges to the satellites and calculate from these values the current position of the receivers antennas phase center. A typical receiver consist mainly out of an antenna with preamplification, a high frequency section for processing of the received signals and a microcontroller for the calculations. Of course, a power supply, a memory storage, a communication interface and a quartz oscillator for the microcontroller clock are needed as well. [8]

The signals sent by the satellites to the receivers contain the carrier, the ranging codes and the navigation messages which can be used by the receiver to retrieve the satellites position and the pseudo range to the satellite. The signals are emitted at two or more frequencies in the L-band, especially in the upper L-band (1.559 GHz - 1.61 GHz) and the lower L-band (1.151 GHz - 1.214 GHz). The specified frequency in these bands resembles the frequency of the carrier. The navigation messages modulated on the carrier are coded with Pseudo-Random Number (PRN) codes which can be used to retrieve the travel time of the signal which is explained in more detail later on. This navigation data consist out of information about the satellite such as its ephemeris, the clock bias, the almanac and the health of the satellite. The messages are binary coded. All GNSS systems use Code Division Multiple Access (CDMA) (except for legacy GLONASS which uses Frequency Division Multiple Access (FDMA)) for the reuse of the same frequency for all satellites. [8]

In order to decrease the influence of Faraday rotation caused by the ionosphere and weather conditions, multipath and other interferences, the radiated signals are circular polarization [26].

In order to get the position, the receiver must know the current position of the satellite and the distance between itself and the satellite. For retrieving the current position of the satellite, the satellite sends ephemeris in their navigation messages to the receiver from

which the coordinates of the satellite can be computed. The travel time of the signal from the GNSS satellite's antenna phase center to the GNSS receiver's antenna's phase center is determined by comparing the reception time of receiver's system time with the GNSS satellite's emission time of the signal. The receiver generates a replica of the CDMA code sent by the satellite and correlates it's replica with the received signal of the satellite. The receiver changes the travel time and frequency offset estimate until a maximum correlation with the satellites code is achieved. From the determined travel time, the distance can be calculated by multiplying with the speed of light  $c$ . This distance is called pseudo range because it is not equivalent to the geometric distance between the satellite and the receiver due to error influences. These errors are the time synchronization error between receivers and satellites clocks, the atmospheric propagation error influenced by the troposphere and the ionosphere, relativistic effects, measurement delays, multipath, and noise. [8]

With only the pseudo range to one satellite the position cannot be determined. With pseudo ranges to two satellites the possible positions can be described by a hyperbola in 2D space and a hyperboloid in 3D space. With an additional satellite the uncertainty can be reduced to two possible positions. For a receiver on Earth's surface the position is even with three satellites unambiguous due to that the second solution is an implausible position far away in space. In figure 8, the described positioning for a GNSS receiver onboard a ship in a 2D plane for three satellites is visualized. The F points mark the positions of the satellites and the stars mark the possible positions for the receiver on the ship. In order to get a good positioning estimate at least four satellites are needed, three for the positioning and one for time synchronization. [8] The algorithms to calculate the position are presented in detail in [8].

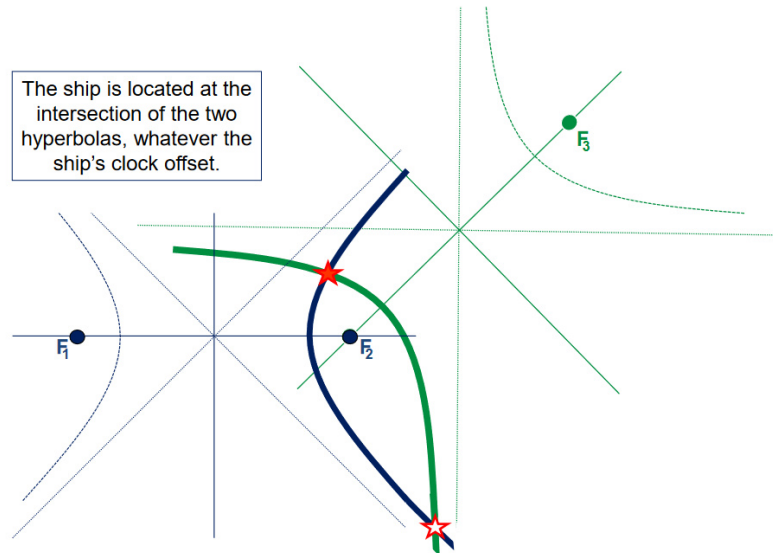


Figure 8: Position determination with three satellites (F) on a 2D plane using hyperbola [8]

The phase center of an antenna is the apparent source of radiation. The position of the

phase center is not the same as the physical center of the antenna and varies with signal frequency and the incident angle of the signals. The phase center offset and the Phase Center Variation (PCV) can be corrected by applying the correction values from antennas ANTEX or SINEX files. These include the phase center offset to the Antenna Reference Point (ARP) for all frequencies, azimuth and elevation angles. The ARP is a fixed point defined by the manufacturer typically at the bottom of the antenna which is used as reference for all position measurements. [8]

A higher precision can be achieved by analyzing the phase of the carrier signal of the GNSS signals done by methods like Precise Point Positioning (PPP) and RTK. Due to its higher frequency compared to the code phase the time can be measured with a higher precision. The RTK positioning technique is explained in more detail in the next chapter. [8]

A more detailed introduction to GNSS systems' functionalities and algorithms is given in [8].

### **2.3.2 RTK and Multi Antenna Sensing for Attitude and Position Determination**

RTK allows a much more precise positioning due to the analysis of the carrier phase over the code phase. Unfortunately, the carrier phase contains an ambiguity which has to be fixed in order to achieve a positioning accuracy of a few millimeters [8]. Thus, the distance between the satellite and GNSS antenna can be expressed in carrier wavelengths. The fractional of this distance resembles the measured carrier phase of the current period. The integer value of the number of wavelengths is unknown and must be determined from the pseudo range and by solving the integer ambiguity [27].

In the RTK method, raw carrier measurement data is received from a reference station with known coordinates. The own carrier phase measurements are compared to the reference station's measurements and the position can be given in relation to the reference station's position. Due to this relative positioning, the influence of propagation errors caused by the troposphere and the ionosphere in the carrier phase as well as the clock biases errors of the satellites can be reduced. If the distance between the reference station and the receiver is below five kilometers and both antennas receive the same GNSS satellites, the atmospheric propagation errors as well as the satellite clock bias can be assumed the same for both receivers and can therefore be neglected. This is resembled by the difference between the measured carrier phase at the reference station and the carrier phase of the same satellite measured at the receiver which is called single reference. The clock bias between the reference station and the receiver can be equalized by the double difference which is the difference between two satellites single references. This leaves only noise errors and multipath errors in the distance determination. The integer ambiguity can be resolved by using a set of double differences for the position estimation. [27]

The integer ambiguity of the distance consists out of an integer number of wavelengths which has to be determined in order to get the position of the receiver [8]. For fixing of the integer ambiguity, the LAMBDA algorithm from Delft university described in [28] can be used which is also implemented in the used GNSS receiver mosaic-go from Septentrio [24]. Another possible algorithm is described in [8].

An approach similar to RTK is used for the determination of the attitude of an object with multiple GNSS antennas. In [9] algorithms for the attitude determination with multiple antennas used in the PolaRx2 receiver from Septentrio are described. In the project of this thesis, a newer GNSS receiver from Septentrio called mosaic-go is used. Because the exact method used in the mosaic-go is not being mentioned, it is assumed that the in [9] described algorithms or advanced versions of them are used in the mosaic-go's attitude calculation as well. These algorithms are presented in the following section:

One method implemented by Septentrio is called direct computation method (DCM) which is similar to the RTK method. The system consists out of one main antenna and at least one auxiliary antenna. The relative position between the main and auxiliary antennas is estimated by a baseline Kalman filter in an ENU reference frame. In this setup the main antenna resembles the base and the auxiliary antennas resembles the rover in a RTK system. In order to achieve a sub-centimeter accuracy of the baseline length, double-differenced carrier phase measurements are done with resolved integer ambiguities by the LAMBDA algorithm. [9]

After the relative position of the auxiliary antenna in perspective to the main antenna is known, the attitude angles can be calculated by direct transformation with the following equations from [9] with  $x_{aux}$ ,  $y_{aux}$  and  $z_{aux}$  as the ENU coordinates of the auxiliary antenna.

$$heading = \arctan\left(\frac{x_{aux}}{y_{aux}}\right) \quad (30)$$

$$pitch = \arctan\left(\frac{z_{aux}}{\sqrt{x_{aux}^2 + y_{aux}^2}}\right) \quad (31)$$

For the determination of all attitude angles, two auxiliary antennas are needed. With only one auxiliary antenna, the heading, and the pitch or roll angle (dependent on mounting of the antennas) can be calculated.

A calibration for this method is not needed and the absolute position does not need to be known in advance. A longer baseline increases the accuracy up to a distance where atmospheric disturbances become prominent. The calculation for the DCM method assumes always a moving platform which results in a longer time for the attitude solution and integer ambiguity resolving for fixed platforms. [9] The following table 2 from [9] shows the determined accuracy of the attitude angles for different baseline lengths determined

with the PolaRx2 receiver:

baseline length	heading accuracy	pitch accu- racy
1 m	0.30°	0.60°
3 m	0.10°	0.20°
10 m	0.03°	0.06°

Table 2: Accuracy of the attitude angles of DCM method determined by PolaRx2 receiver [9]

The second algorithm for attitude determination described in [9] is the quaternion based Kalman filter. This method determines the attitude from the double-differenced carrier phase measurements of multiple auxiliary antennas with quaternion parameterization. Due to the requirement of the auxiliary antenna positions that shall be known apriori, this algorithm cannot be used for the measurement instrument because the instrument shall determine the position of the auxiliary antennas in perspective to the main antenna by itself. Therefore, the algorithm is not covered in this thesis. For further information about this algorithm refer to [9].

### 3 State of the Art

A project which uses the GNSS multi antenna method described in chapter 2.3.2 in combination with a Micro Electro Mechanical System (MEMS) gyroscope for the determination of the attitude of a vehicle is explained in [29].

In the project three GNSS antennas and one MEMS-Inertial navigation system (INS) are used to determine the attitude. The antennas are placed in a L-shape on the vehicles roof forming two baselines. One baseline is directed in the driving direction and determines the yaw and pitch angle of the vehicle. This baseline has a length of 2.5 meters. The second baseline with a length of 1.3 meters is orthogonal to the vehicle and allows the determination of the roll angle. The MEMS-INS gyroscope with an accuracy of  $<0.01$  degrees is used for improving the fixing of the ambiguities as well as the increase of the accuracy and reliability of the attitude. The attitude measurements of both sensor system are combined in a sensor fusion with an extended Kalman filter. The described system is tested in an agricultural and urban environment. The L1 and L2 carrier phases of GPS are used for the attitude determination. In the agricultural environment with good satellite visibility a standard deviation ( $1\sigma$ ) of the yaw angle of 0.052 degrees, of the pitch angle of 0.105 degrees and of the roll angle of 0.169 degree can be achieved with the proposed GPS system. With the use of the extended Kalman filter the standard deviation can be reduced to  $0.033^\circ$  for the yaw angle, to  $0.081^\circ$  for the pitch angle and to  $0.130^\circ$  for the roll angle. [29]

In [30] an experiment using low cost GNSS receivers and antennas is explained. It provides an optimized algorithm based on the LAMBDA method for attitude determination which allows faster fixing of ambiguities and improved accuracy of the attitude angles. Multiple single frequency receiver are used in order to achieve the performance of a multi frequency receiver. The algorithm uses multiple baselines and the LAMBDA method for determination of the attitude. Only GPS and Beidou satellites are used for attitude determination. Three low cost receivers with patch antennas are located in a triangle shape with different baseline lengths. For the experiment the direct calculation method is used for the calculation of the alignment. An accuracy of  $0.07^\circ$  for the yaw angle,  $0.12^\circ$  for the pitch angle and  $0.16^\circ$  for the roll angle at a baseline of 2 meters can be achieved with the proposed method. [30]

The same precision seen in these two projects shall be achieved with the measurement instrument developed in this thesis. Similar to the project from [29], the attitude determination is based on the multi antenna method described in chapter 2.3.2 but only two antennas are used by the instrument described in this thesis. Therefore only two angles can be determined. A MEMS sensor is used as well but rather an inclinometer than a gyroscope due to low movement speeds of the corner reflector which is quite static in comparison to a car. A sensor fusion is not done for the angles of the alignment in this

thesis. Instead the values with the better accuracy are displayed as final alignment angle. Similar to the project from [30], the multi antenna method and the LAMBDA method described in chapter 2.3.2 are used by the GNSS receiver in this thesis. Instead of using low cost single frequency receivers described in the project, only one multi frequency receiver is used in this thesis. Another deviation is the usage of only two antennas and an inclinometer for the determination of the alignment angles instead of multiple antenna baselines.



## 4 Developement of the Alignment Measurement Instrument

A measurement instrument shall be developed which determines and provides the current alignment of trihedral and dihedral corner reflectors as well as the exact position of the phase center of the corner reflector. It shall be a mobile, light weighted, small and easy to mount instrument. The azimuth and the elevation angle of the trihedral corner reflector and, for the dihedral corner reflector, the azimuth, elevation and the roll angle of the reflector shall be determined. An accuracy of the attitude angles of below  $0.5^\circ$  and an accuracy of the position of the phase center of a few millimeters shall be achieved. The instrument shall provide the data via a web interface and shall provide an interface for user's input. The selection of the components shall be done with attention to short lead times and long availability in the future. The device shall be designed for a low power consumption and use a rechargeable power source. There shall be a possibility to store the alignment data and position on the device in order to update the alignment angles of the corner reflectors in DLR's database when returning from a alignment campaign. The device shall be able to allow user input for the reflector's ID and calibration site as well as the reflector's size if it cannot be determined by the device itself.

The design and manufacturing of the housing of the device and the fixations for the GNSS antennas is task of the mechanical department and the workshop. The requirements for the fixations and the housing shall be discussed with the mechanical department and the proposed design shall be reviewed. The components of the measurement instrument shall be placed in the housing with space and wiring efficient. Therefore, the positioning of the components and elements such as connectors and jacks inside the housing shall be proposed to the mechanical department and the feasibility of the proposal shall be discussed. In the following chapter, the concept of the measurement instrument is presented and described which fulfills all the above defined requirements for the device.

### 4.1 Concept of the Instrument

The alignment measurement for the corner reflector is based on a GNSS receiver and a two axis inclinometer. The GNSS receiver is used to determine the heading of the corner reflector and the accurate position of the main and auxiliary antenna. From these positions, the position of the phase center of the corner reflector is calculated using the inclinometer to measure the alignment angles pitch and roll.

In the following sections, the concept of the measurement instrument is explained in more detail. The concept for the fixation of the antennas and the measurement instrument on the corner reflectors is presented. After that, the hardware and software concepts are described.

#### 4.1.1 Positioning of the GNSS Antennas

For the attitude determination, the GNSS antennas need to be mounted on the corner reflector. Therefore, fixations are built by the workshop. The fixations allow to separate the GNSS antennas from the metal plates of the corner reflector to avoid interferences due to multi-path effects. The fixations shall be easy and fast to mount in order to allow a short setup time for the measurement instrument. The detailed design and manufacturing of the fixations is done by the workshop. The placement of the antenna's fixation and the measurement instrument on a trihedral corner reflector is depicted in figure 9 and is described hereinafter.

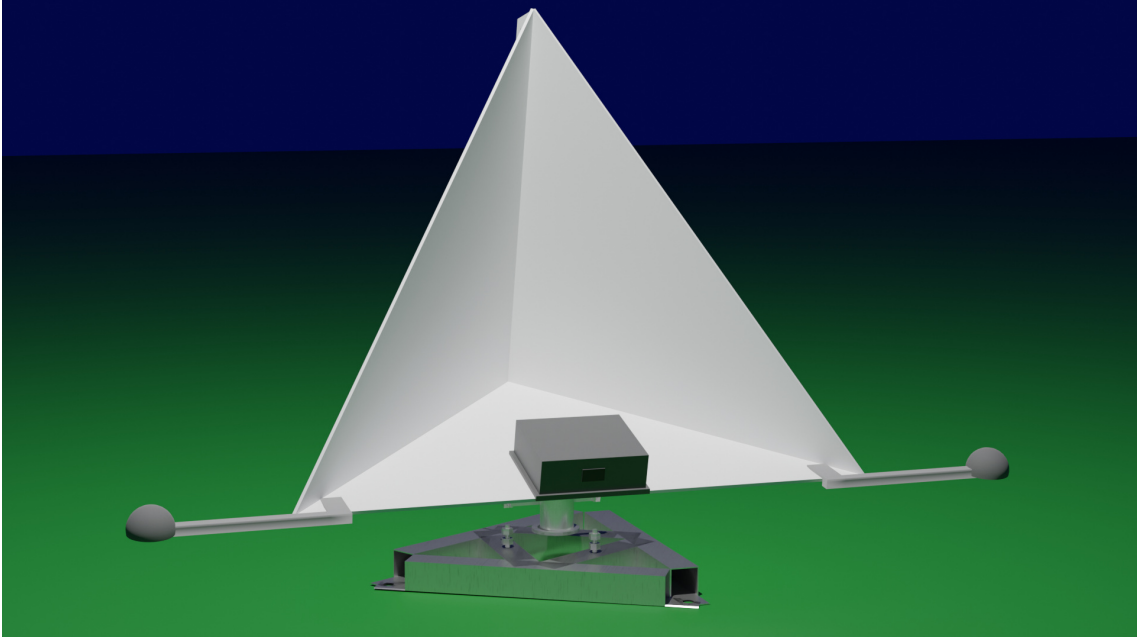


Figure 9: Trihedral corner reflector with antenna fixations and measurement instrument

The accuracy of the attitude angles improves with an increasing baseline between the two GNSS antennas as seen in chapter 2.3.2. Therefore, the antennas should be placed as far away as possible from each other under the condition that a stable mounting can still be ensured. The longest baseline for a trihedral corner reflector can be achieved by mounting the antennas fixations at the reflector's vertices. The resulting baseline length can be derived from the trihedral corner reflector's geometry with the following equation:

$$l_{baseline} = \sqrt{2}l_{inner} + 2l_{fixation} \quad (32)$$

The length of the fixation is selected as 50 centimeters from the corner of the reflector to the antenna's reference point leading to a baseline length of approximately two meters for the smallest corner with an inner edge length of 70 centimeters. For this baseline length, an accuracy of the heading angle of  $\approx 0.075^\circ$  and an accuracy of the pitch / roll angle

of  $\approx 0.125^\circ$  can be achieved with the used GNSS receiver from Septentrio under ideal conditions [31].

In order to allow a good satellite visibility for the GNSS antennas at all alignment angles, a position outside of the reflector is chosen for the fixation of the antennas. From the GNSS baseline measure, the azimuth angle can be derived from the yaw angle by adding or subtracting 90 degrees depending on the definition of the main and auxiliary antenna [24]. The elevation angle measured by the instrument is the elevation of the baseplate. The bore sight elevation angle is calculated from the baseplate elevation angle by adding an offset of approximately 35.26 degree as described in chapter 2.1.2. In DLR's case, the typical elevation angles for the bore sight lie in between 40 and 70 degrees. To achieve a good satellite visibility in this range, the antennas are tilted by 20 degrees with respect to the baseplate to the front. In this configuration, the antennas are pointing to the zenith at a bore sight elevation angle of approximately 55 degrees which is exactly the middle of the typical interval.

The measurement instrument is placed in the middle of the baseplate for a trihedral corner reflector. It can be attached to the front edge of the reflector. A metal plate is used to establish a planar and large contact area with the corner reflector to ensure the accuracy of the measurement of the inclinometer. On this metal plate the inclinometer is mounted as far away as possible from the edge of the corner reflector near the support structure because the edges of the corner reflector are often deformed due to action of forces during the manual alignment. These deformations would negatively influence the measured tilt angles.

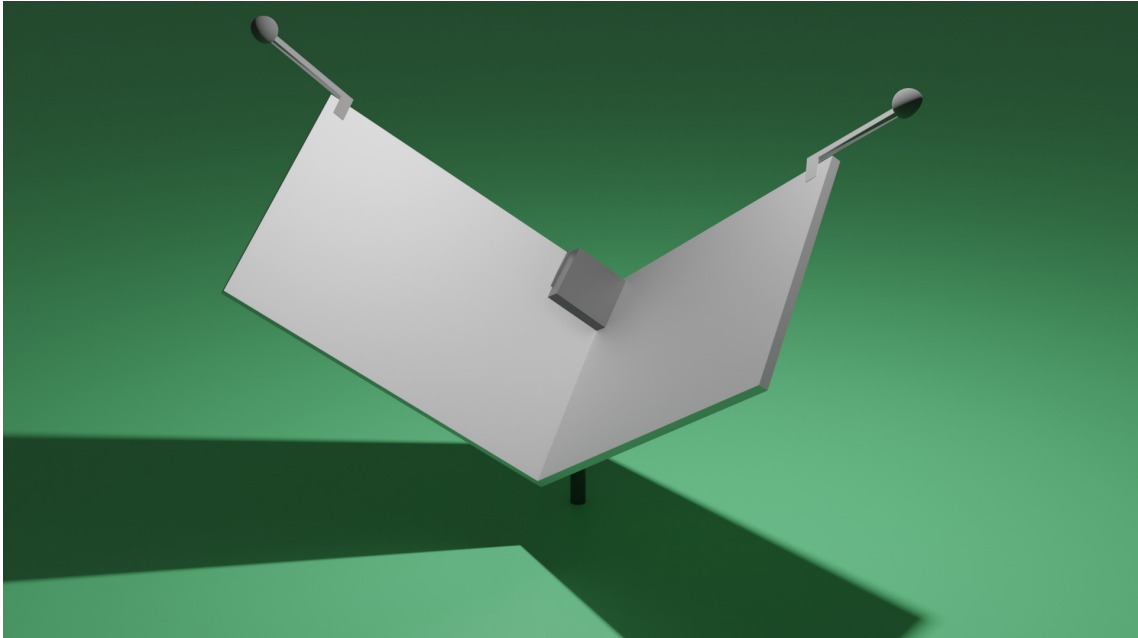


Figure 10: Dihedral corner reflector with antenna fixations and instrument housing for the electronics

The placement of the measurement instruments and the antennas is shown in the dihedral corner model in figure 10. For the dihedral corner reflector the longest possible baseline is the diagonal between the two plates corners. Unfortunately, at some alignments the satellite visibility is reduced for one of the antennas due to the metal plate above the antenna. Due to this reason, the antennas are mounted at the corner of each plate on the same side of the reflector which is pointing to the sky. The baseline length can be calculated from the geometry of the dihedral corner reflector with the following equation under the condition that the length of the fixation is an extension of the length of the plates:

$$l_{baseline} = \sqrt{2}(l_{plate} + l_{fixation}) \quad (33)$$

The typical roll angle of the dihedral corner reflector is, in DLR's use case, 22.5 degrees or 45 degrees. For the dihedral corner reflectors, the measurement instrument is placed at the edge near the phase center line at one of the two plates.

#### 4.1.2 Hardware Concept

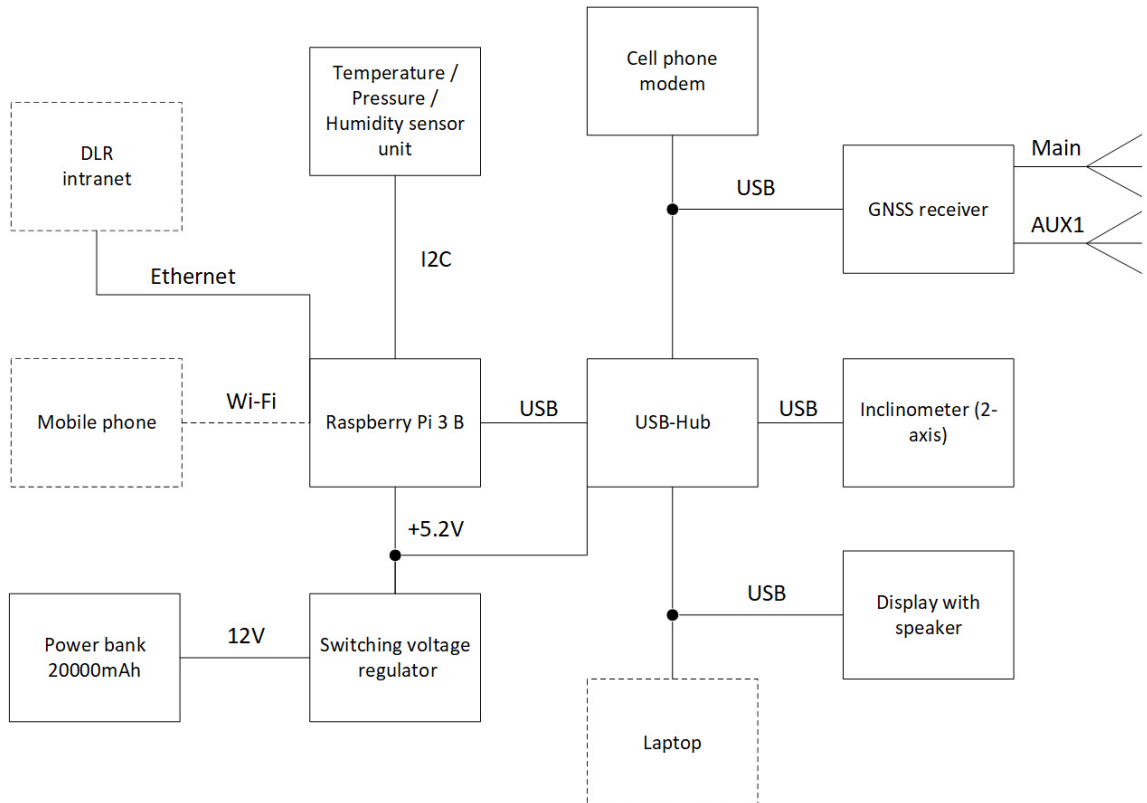


Figure 11: Block diagram of the measurement instrument

The measurement instrument consists mainly of the GNSS receiver with a main and an auxiliary antenna, a two axis inclinometer, a microcomputer (Raspberry Pi 3 B), an en-

vironment sensor and a display. The hardware structure is shown in the block diagram in figure 11. For the power supply of the device, a 5.2 Volt switching voltage regulator as well as a power bank is used. The power bank provides a 12 V output to supply the voltage regulator and a 5V Universal Serial Bus (USB) output. The complete measurement instrument draws a current of 2.3 A in worst case. A 20 Ah (at 3.7 V) power bank is used to supply the circuit, in worst case, for more than six hours. Keeping in mind that the measurement instrument is only operated for a short period of time, this battery lifetime is more than sufficient for an entire working day of measurements. To provide a higher stability of the supply voltage, a 5.2 V voltage regulator is used. The 5.2 V includes a margin of 0.2 V for voltage drops on the supply cables so that the supply of the Raspberry Pi with 5 V is always ensured.

The Raspberry Pi comes with an ethernet jack, a Wi-Fi interface and four USB slots. All USB connections can in total supply up to 600 mA which is in worst case not enough for all peripheral devices. Therefore, an active USB-Hub is used to provide additional connectors for more devices as well as guarantee a good current supply to all peripherals. The ethernet connection is used to connect the device to DLR's intranet allowing the transmission of measured data to DLR's database. The Wi-Fi interface can be configured as an access point to connect mobile phones to the Raspberry Pi in order to view the measured data on a web interface. Additionally, the Raspberry Pi is used to calculate the corner reflector's attitude angles and the corner reflector's phase center position.

The GNSS receiver is connected to the Raspberry Pi via an USB connection. The receiver allows ethernet over USB to allow faster connection speeds than the pure serial connection over USB. The receiver applies the RTK algorithm and multi antenna method as described in chapter 2.3.2 to measure and calculate a precise position of the main and auxiliary antenna as well as the alignment of the baseline of the two antennas.[24]

A mobile phone modem (Long Term Evolution (LTE)) is used to provide internet connection for the device in the field via cellular radio. The GNSS receiver is connected to an online *Networked transport of RTCM via Internet Protocol (NTRIP)* caster which is used to receive correction data, known as RTCM messages, from a nearby base station for the RTK positioning of the receiver.

The inclinometer uses a MEMS sensor to provide the tilt angles for two axis in the range of -90 degrees to 90 degree from the horizontal. The inclinometer can be accessed by the Raspberry Pi over an USB serial interface. [32]

The environmental sensor is connected to the Raspberry Pi via a Inter-Integrated Circuit (I2C) interface and provides the current temperature, pressure and humidity. The temperature can be used to apply thermal corrections and compensations on the measurements.

The display shows the attitude of the corner reflector as well as the position of the phase center to the user as back up so that aligning of the corner reflector is possible even if

no mobile phone is available. The speaker of the display can be used as proximity sensor to support the alignment process. The desired alignment angles can be entered, and the speaker provides feedback how close the current alignment is to the desired one by different pulse lengths which is not yet implemented.

#### 4.1.3 Software Concept

The software of the measurement instrument shall follow a modular design to allow a reuse in different projects. Therefore, for every major component such as the GNSS receiver, the inclinometer, the display, the webserver's interface and the environment sensor a own module with a representative class is created. Additionally, a module for the calculation of the corner reflectors azimuth, elevation and phase center is implemented. A main program is used to redirect the data between the module's classes and to control the operation of the measurement instrument. The modules and classes are implemented in Python. In figure 12, the classes with their most important methods and their relations between each other is displayed. The functionality of each class as well as the concept of operation is described in the following section.

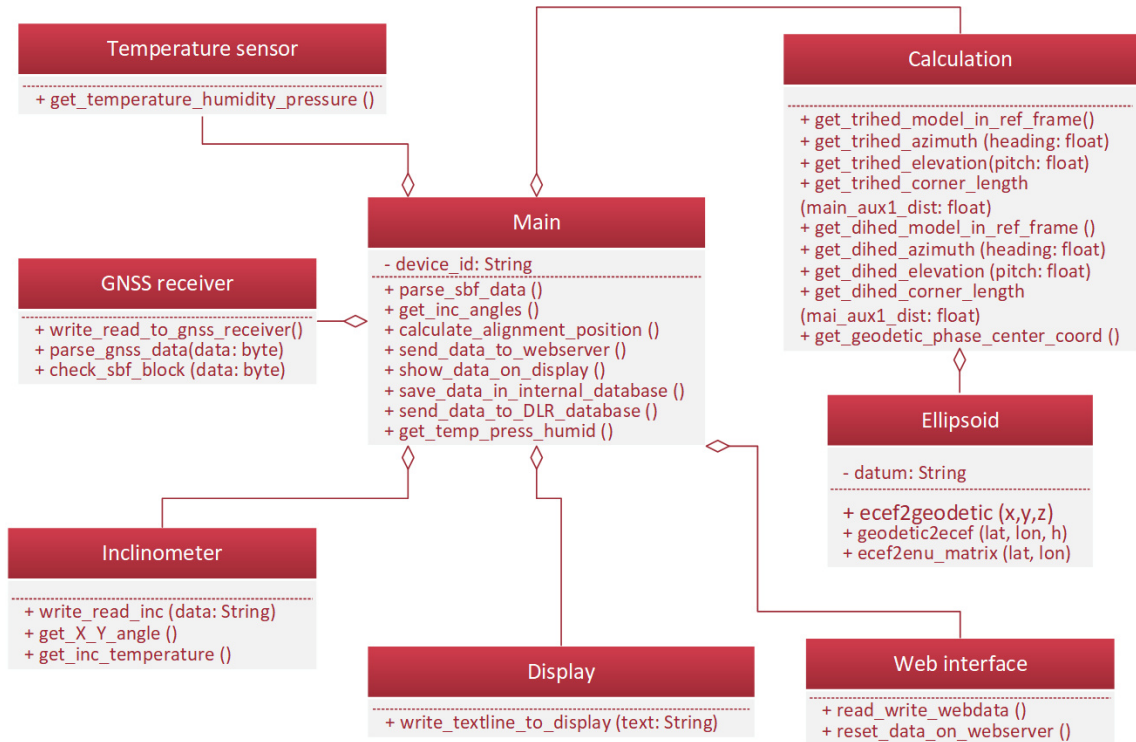


Figure 12: UML class diagram of the measurement instrument

#### GNSS Receiver

The GNSS receiver class is used for the communication with the receiver from Septentrio. The communication can be established over a serial connection via USB or by an ethernet connection over USB. The ethernet connection has the advantage that it is much faster

than the serial connection. The ethernet over USB connection additionally allows the receiver to connect to the internet if IP forwarding is allowed on the connected device. With this internet connection, the receiver can log into a NTRIP caster which provides a connection to an NTRIP server. From this server, correction data for the RTK algorithm from a nearby base station can be received. The correction data is received in the RTCM format. The receiver automatically processes the correction data and applies it to its RTK method in order to achieve a position accuracy in the order of millimeters.

The receiver from Septentrio calculates the antennas position and the attitude angles of the baseline between the main and the auxiliary antenna with the algorithms described in chapter 2.3.2. Due to the use of two antennas, only the heading and the pitch angle can be calculated by the receiver. For the GNSS antenna's phase center offset and variation described in chapter 2.3.1 the GNSS receiver provides a list with correction values for the different GNSS frequency bands for different antennas. An antenna from this list is selected for the application in order to mitigate the influence of phase center variations on the accuracy of the GNSS position measurements. Other methods applied by the receiver to improve the accuracy of the measurements are the estimation of the ionosphere and troposphere delays for the electromagnetic waves from the GNSS satellites. [24]

The receiver allows to provide its data in different formats. The Septentrio Binary Format (SBF) block format is Septentrio's own binary format which provides all information of the receiver in compact sorted blocks. The data from the receiver can be received in National Marine Electronics Association (NMEA) sentences which only provide a limited part of the GNSS receiver's data. The output data can be sent by the receiver once or in fixed time intervals. [24]

Regarding the communication process with the GNSS receiver, first the configuration commands for the receiver are loaded from a configuration file and it is tried to establish a connection to the receiver over ethernet over USB. If successfully connected, the commands are sent to the receiver and the answer is read back and stored in a buffer. The data in the buffer is checked for the symbols indicating the start of a response as well as for the symbol of the next message in order to ensure that the complete message has been received. This message is then removed from the buffer and checked for the type of message. These message types can be responses with success or error message for the sent command, American Standard Code for Information Interchange (ASCII) messages with information or receiver events, formatted information blocks, NMEA sentences, Simple Network Management Protocol (SNMP) binary command replies, and SBF blocks. The type of message is indicated by an identifier symbol. Not used message types are stored in queues for possible usage in other projects. If a SBF block is detected, it is checked for the correct length, checksum, and identifier. A successful recognized SBF block is stored with its identifier and it's binary content in a queue. The main program then retrieves the data from the queue and parses it in order to extract the needed data from the block.

In order to ensure real-time capability, multi-threading and sub processing is used. The communication with the GNSS receiver runs as sub process to avoid time loss by waiting for a new SBF block to be received. The handover of the SBF block data to the main program is done by a process safe queue. To avoid a too large backlog in the queues, a new SBF block is put in the queue when the previous block has been processed by the main program. After the storage of the information in the queue, the next command is written to the receiver and the response is read back. This process is visualized in the flow chart diagram in Appendix A.1 in figure 25.

### **Inclinometer**

The inclinometer interface provides functions for writing commands to the inclinometer and reading back the requested information such as the tilt angles, the angle offsets from the factory calibration and the microcontroller temperature for monitoring. Additionally it is possible to set a current angle as offset.

### **Temperature Sensor**

The temperature sensor interface establishes a connection to the sensor and sends the command for retrieving of a tuple of the temperature, pressure, and humidity values from the same measurement epoch. The three values are then returned to the main program for further processing.

### **Ellipsoid**

The ellipsoid module includes the functions to transform ECEF to elliptic geodetic coordinates and vice versa as well as the transformation matrix for the transformation between the ENU and the ECEF coordinate systems as described in chapter 2.2. The module is used by the calculation module to transform the phase center position of the corner reflectors into the elliptic coordinates representation form.

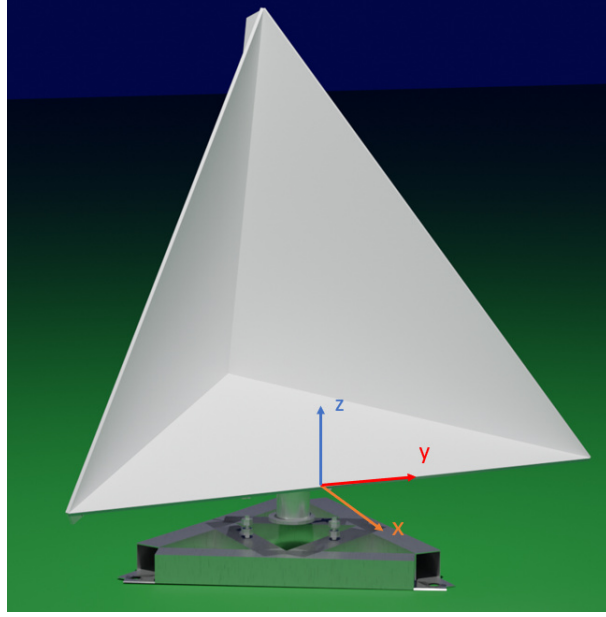
### **Calculation**

The calculation module contains the creation of the reference models for the trihedral and dihedral corner reflector, the calculation functions for the azimuth and the elevation angle of the corner reflector, functions to calculate the corner reflector size from the antennas baseline length and the functions to transform the corner reflector's model from the reference model frame to the ENU coordinate frame and afterwards to the geodetic coordinate frame.

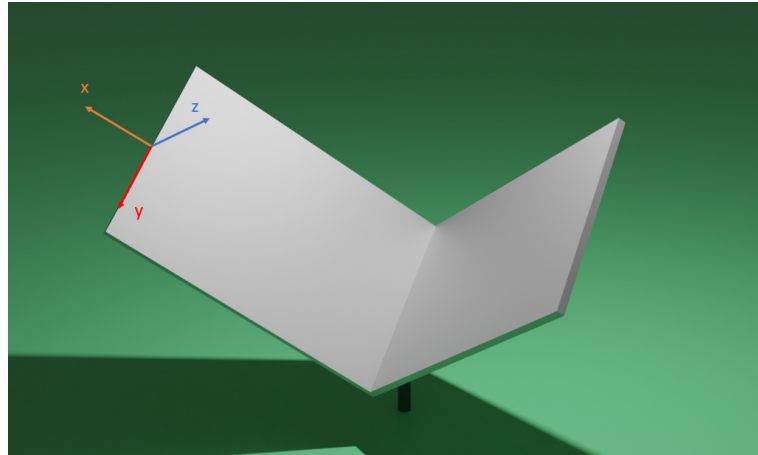
The size of the corner reflector is estimated by the evaluation of the baseline length and comparison with valid corner lengths from a configuration file. In order to estimate the length for a dihedral corner reflector, the width of the reflector must be known and input



to the system. The function then compares the derived length from the baseline and the width with valid combinations from a configuration file.



(a)



(b)

Figure 13: Corner reflector models with reference coordinate system:

(a) trihedral corner reflector model and

(b) dihedral corner reflector model

By knowing the size of the corner reflector as well as the positions of the GNSS antennas and their baseline, the position of the corner reflector's phase center cannot be determined and is ambiguous due to different possible orientations of the reflector's baseplate. Additional information about the orientation of the corner reflector is needed. On the other hand, the inclinometer provides the orientation of the baseplate but not the position in the three dimensional space. Therefore, in order to obtain the position of the phase center, the problem is approached in a different way. A virtual reference model of the corner reflector with the known position of the phase center is created. This model is trans-

formed so that the GNSS antenna's positions and the baseplate angles from the virtual model are fitted with the measured positions and attitude angles. By transforming the known phase center position of the virtual model, the phase center position can directly be determined for the transformed model as well. To implement this approach, a virtual reference model of the corner reflector is created. For the trihedral corner reflector, the origin of the reference coordinate system is located in the middle of the outer edge of the baseplate which is referred to as reference point. The x-axis is pointing from the reference point in the opposite direction of the phase center. The z-axis is defined upwards from the reference point which resembles the normal to the baseplate. From these definitions, the y-axis is pointing to the left of the x-axis in order to form a right-handed-coordinate system. The trihedral corner reflector's reference coordinate system definition is shown in figure 13a.

For the dihedral corner reflector, the origin is defined in the middle of the outer edge of one of the two plates which is also referred to as reference point. The definition of the reference coordinate system is the same as for the trihedral corner reflector and can be seen in figure 13b.

This reference model is then used as input for a least square optimizer which tries to find the transformation from this reference coordinate frame to the ENU coordinate frame. The positions of the main and auxiliary antenna are known in the ENU frame. The position of the auxiliary antenna is provided by the GNSS receiver in ENU coordinates in respect to the main antenna. Due to this, the main antenna can be used as origin of the ENU frame in order to use the relative coordinates of the auxiliary antenna with respect to the main antenna returned by the receiver directly for the representation of the reflector in the ENU frame. The optimizer tries to fit the positions of the antennas in the reference frame to the antenna's positions in the ENU frame by rotating the model around the x, y and z-axis in the global Euler convention order as well as by translating the model in the three coordinate axis directions. The transformation follows the mathematical principles explained in chapter 2.2.3. Unfortunately with the two antenna positions known, only two alignment angles for yaw and roll can be fixed which leads to ambiguities of the position of the virtual model in the ENU frame. In order to fix this ambiguity, the pitch angle information must be included in the error function of the optimizer. There are different ways to check the deviation of the pitch angle of the transformed corner reflector to the pitch angle measured by the inclinometer. The different algorithms for the error function are described and evaluated in detail in chapter 5.3.1. For the optimizer the error function algorithm is selected which is showing the best results during the instrument validation. The comparison and validation of the different algorithms for the error function of the optimizer is presented in chapter 5.3.1.

All these error function algorithms have in common that the angle of the baseplate to the coordinate planes need to be determined. The angles can be calculated by using vector

projections and the arctangent function to get the angles unambiguous. The projection can be seen in figure 14 for the example of determining the angle of the baseplate to the x-y plane. This angle  $\alpha$  in figure 14, can be calculated with following equations with  $\vec{bp}$  as vector of the baseplate pointing from the phase center to the outer edge of the corner reflector and  $\vec{e}_u$  as unit vector of the u axis:

$$\vec{P}_{up} = (\vec{bp} \cdot \vec{e}_u) \vec{e}_u \quad (34)$$

$$\vec{P}_{north} = \vec{bp} - \vec{P}_{up} \quad (35)$$

$$\alpha = \arctan2\left(\frac{|\vec{P}_{up}|}{|\vec{P}_{north}|}\right) \quad (36)$$

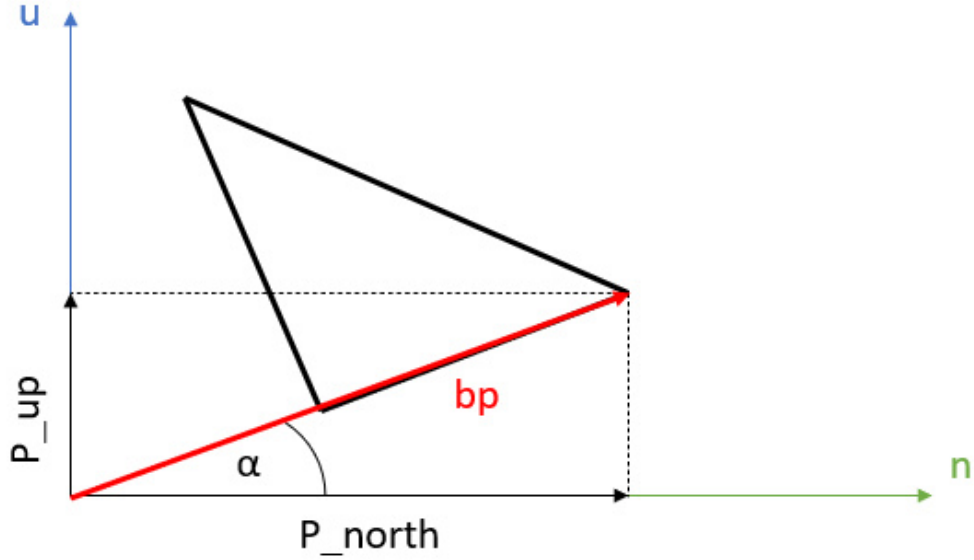


Figure 14: Projection of phase center vector of corner reflectors baseplate

Once the model is fitted to the ENU coordinate frame, the ENU coordinates of the corner reflectors phase center can be retrieved. The phase center coordinates can then be transformed to geodetic coordinates with the functions from the ellipsoid class. The calculation of the phase center position runs in a thread due to the time of a few seconds needed by the optimizer to fit the transformation parameters. When a new position has been calculated it is returned in a queue to the main program.

Additionally, the azimuth and elevation angle are determined from this transformed model. The front three vertices at the opening of the corner reflector describe a plane. The normal vector of this plane is pointing in the same direction as the bore sight of the corner reflector. With projections, the elevation and the azimuth angle with respect to

the ground can be calculated from this bore sight vector with the following equations with  $\vec{n}$  as bore sight vector,  $n_{east}$  and  $n_{north}$  as north and east component of the bore sight vector and  $\vec{e}_u$  as unit vector of the u axis:

$$\vec{P}_{up} = (\vec{n} \cdot \vec{e}_u) \vec{e}_u \quad (37)$$

$$\vec{P}_{north} = \vec{n} - \vec{P}_{up} \quad (38)$$

$$elevation = \arctan2 \left( \frac{\vec{P}_{up}}{|\vec{P}_{north}|} \right) \quad (39)$$

$$azimuth = \arctan2 \left( \frac{n_{east}}{n_{north}} \right) \quad (40)$$

Another method to calculate the azimuth and elevation angle for the trihedral corner reflector is by directly applying the offsets from the known corner reflector's geometry to the measured pitch and heading angle. For the dihedral corner reflector this method cannot be used to calculate the alignment angles due to dependency of the corner reflectors elevation angle to the pitch and the roll angle. This correlation can be seen when rotating the reflector by a pitch angle of 90 degrees and rotating afterwards by a roll angle of 45 degrees. The elevation angle will not be 90 degrees but depend on both components of the pitch and roll angle. Both methods, the projection method and the offset method, for the alignment calculation are evaluated for the trihedral corner reflector and the results of both methods are compared in chapter 5.

## Web Interface

On the webserver a frontend, a backend and a Representational State Transfer (REST) Application Programming Interface (API) for communication with the application is implemented. The frontend appears as graphical user interface on the users mobile phone and reads in certain intervals the data from the webserver's backend and updates its displayed values. If there is an input from the user, the frontend writes the change to the backend. On the backend of the webserver, the data is stored in a database. Over a REST API the frontend and the application can access the database and change the values. The concept of the webserver is displayed in figure 15.

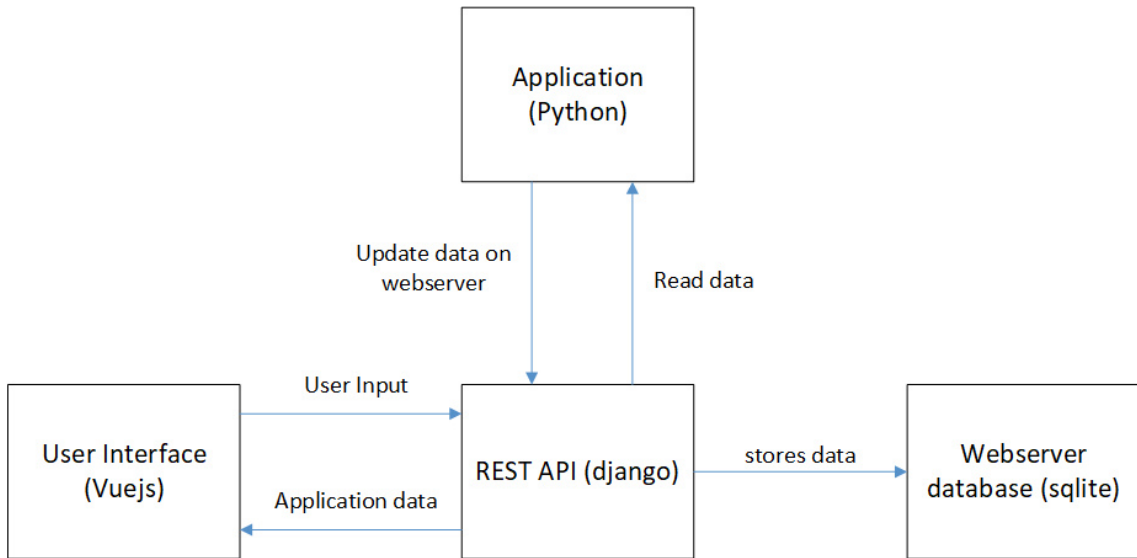


Figure 15: Structure of the webserver

The web interface methods allow the communication with the REST API of the webserver in order to read and write data to the webserver's database. With the functions of this class, the alignment angles and the phase center position can be provided on the frontend for the user and user's inputs can be received. The application tries to read data from the webserver's database over the REST API. If the connection could not be established successfully, the function returns the error code to the main routine. If the accessed database element does not exist, the application will post the element on the webserver. If the element does exist, the read data will be put in a queue for processing by the main program and the new data will be handed over to the REST API in order to store the data on the webserver. The status code is checked for a successful update of the values. Due to long access time for a webserver request, the web interface module runs in a thread as well. The data of the webserver is read to a queue and the data from the main program is written cyclically from a queue to the webserver.

## Display

If the webserver is not used (e.g. due to connection problems or due to no availability of a mobile phone), a display can be used as backup for visualization of the alignment angles and the phase center position. The display module provides functions to write commands and text lines to the display over a serial interface.

## Main

The main program is responsible for:

- the evaluation and redirection of the data of all sub modules as well as controlling the operation of the measurement instrument.

- reading the configuration file and the initialization of all other sub modules.
- parsing of the SBF blocks provided by the GNSS receiver module and retrieving of the position of the main antenna in ECEF and geodetic coordinates as well as the position accuracy, the position of the auxiliary antenna in ENU coordinates relative to the main antenna, the heading and the roll angle with their estimated accuracy as well as the GNSS time in Coordinated Universal Time (UTC).

The GNSS time is used to synchronize the system time if no internet access is available in order to provide correct time stamps for saved data. Additionally, debug and other useful information such as the Position Velocity Time (PVT) calculation method (RTK) and error codes can be extracted from the SBF blocks.

The current angles from the inclinometer are read. If a corner reflector size is available and the measurement is started by the user, the antenna's positions, the heading angle from the GNSS receiver and the pitch and roll angle of the inclinometer are handed over to the calculation routine to calculate the geodetic phase center position of the corner reflector. The azimuth and the elevation angle are calculated with the projection and offset method. The calculated values are sent as update to the display and the web interface. The response from the webserver is checked for user inputs like, among others, the corner sizes, flag for the storage of the data and the flag for shutting down the device. If the storage flag is set, the data is collected and stored in the internal database on the device.

Finally, before repeating the measurement cycle, it is checked if the ethernet cable is connected to the device and the DLR intranet network is detected. If a connection to DLR's network is established, it compares the timestamps of the last alignments in the DLR database with the timestamps in the internal database. If the internal database contains more recent data, the respective elements in the DLR database are updated. Currently only the check of the availability of the ethernet connection and the check of the assigned IP to the device by the network is implemented. The transfer of the data to DLR's database is not yet implemented. The sequence of the main program is displayed in the flow chart in Appendix A.1 figure 26.

## 4.2 Hardware Implementation of the Concept

The main component of the alignment measurement instrument is the GNSS receiver. For this component the mosaic-go receiver from Septentrio is used. It provides a horizontal accuracy of 0.6 cm and a vertical accuracy of 1 cm for the position when using the RTK method. For the attitude angles determined by the receiver an accuracy of  $0.15^\circ$  for the heading and of  $0.25^\circ$  for the pitch/roll angle is specified at a baseline length of 1 m. For a longer baseline of 5 meters, the accuracy of the heading improves to  $0.03^\circ$  and the pitch/roll angle accuracy improves to  $0.05^\circ$ . For the baseline length of 3 meters, which

is the expected baseline length for 1.5-meter trihedral corner reflectors with the antenna fixation's lengths, an accuracy of the heading of  $0.05^\circ$  and of the pitch/roll of  $0.08^\circ$  can be expected from the receiver. All these values are specified under the condition of an open sky. [31]

In order to use RTK positioning, the correction data of a base station is accessed via internet by connecting to the NTRIP caster SAPOS. The nearest antenna is selected (VRS\_3G in case of the measurement instrument) as mounting point of the caster for retrieving the RTCM v3 correction data. The data is received in the ETRS98/DREF91 reference frame [20]. The connection to the internet in the field is provided by a LTE modem.

As for the antennas, the TW7972 from Tallysman is selected due to a tight phase center variation and a good multipath rejection. Additionally, the antenna provides filters against intermodulation and saturation caused by 700 MHz LTE signals and a 32dB Low Noise Amplifier (LNA). To protect the receiver's antenna inputs, 3dB attenuators are used in the RF signal line. The antennas are suitable for the Septentrio GNSS receiver and correction data for the antenna's phase center and phase center variation is available in the receiver's internal database. Support structures are built by the workshop to mount the antennas at the edges of the corner reflectors. [33]

Another important component is the inclinometer which measures the pitch and roll angle of the baseplate. The 2-NSDOG2-021 from TE-Connectivity is selected with a measurement range of  $\pm 90$  degrees in two axis with an accuracy of  $0.2^\circ$  at room temperature and an accuracy of  $0.6^\circ$  over the entire temperature range from  $-40^\circ\text{C}$  up to  $85^\circ\text{C}$ . It is assumed that the high deviations are seen near the specified temperature limitations. Due to the usage of the inclinometer in the application in a smaller temperature range of only  $-10^\circ\text{C}$  up to  $70^\circ\text{C}$ , the inclinometer is validated over temperature and the deviation from the angle at  $25^\circ\text{C}$  is calculated. The measurement setup and results of this test are described later in chapter 5.3.1. [32]

For the alignment and phase center position computation, a Raspberry Pi 3 is selected due to its flexibility with interfaces like Wi-Fi, ethernet, USB and configurable GPIOs. The Wi-Fi is operated as access point allowing mobile phones to connect to the Raspberry Pi. A webserver (Nginx) is setup with its backend programmed in 'django' and its frontend written in 'VueJs'. As communication between the webserver and the application the django REST framework is used.

The EA PLUGL128-6GTC from Electronic Assembly is selected as display. It provides an OLED screen and a speaker to output sound pulses. The display provides a variety of interfaces for control such as USB, RS232, SPI or I2C. Additionally, it provides a touch interface allowing for user inputs for future functionalities. The sound functionality can be used in future application for indicating the proximity of the current alignment to an entered one. [34]

As power supply, a power bank is used with a 12 V output. Due to an instability in the voltage supplies of the power bank, a switching voltage regulator is used to convert the 12 V down to a stable 5.2 V power supply. The current consumption of the entire measurement instrument is measured as 1.9 Amperes. For the used power bank with a capacity of 20000 mAh (at 3.7 V) a runtime of 7.81 hours can be achieved. Due to a short alignment time for a single corner reflector, the runtime is sufficient for a whole working day of measurements. The power bank provides a charging adapter for cars to allow charging in the field when driving to the next corner reflector site. The power bank provides a 5 V output for the charging of mobile phones as well, so that the mobile phone can be charged during the measurement to always allow the connection to the web interface of the measurement instrument.

A housing is constructed and built by the workshop for protection of the device against environmental influences such as rain and snow. The described implementation of the measurement instrument is displayed in figure 16.

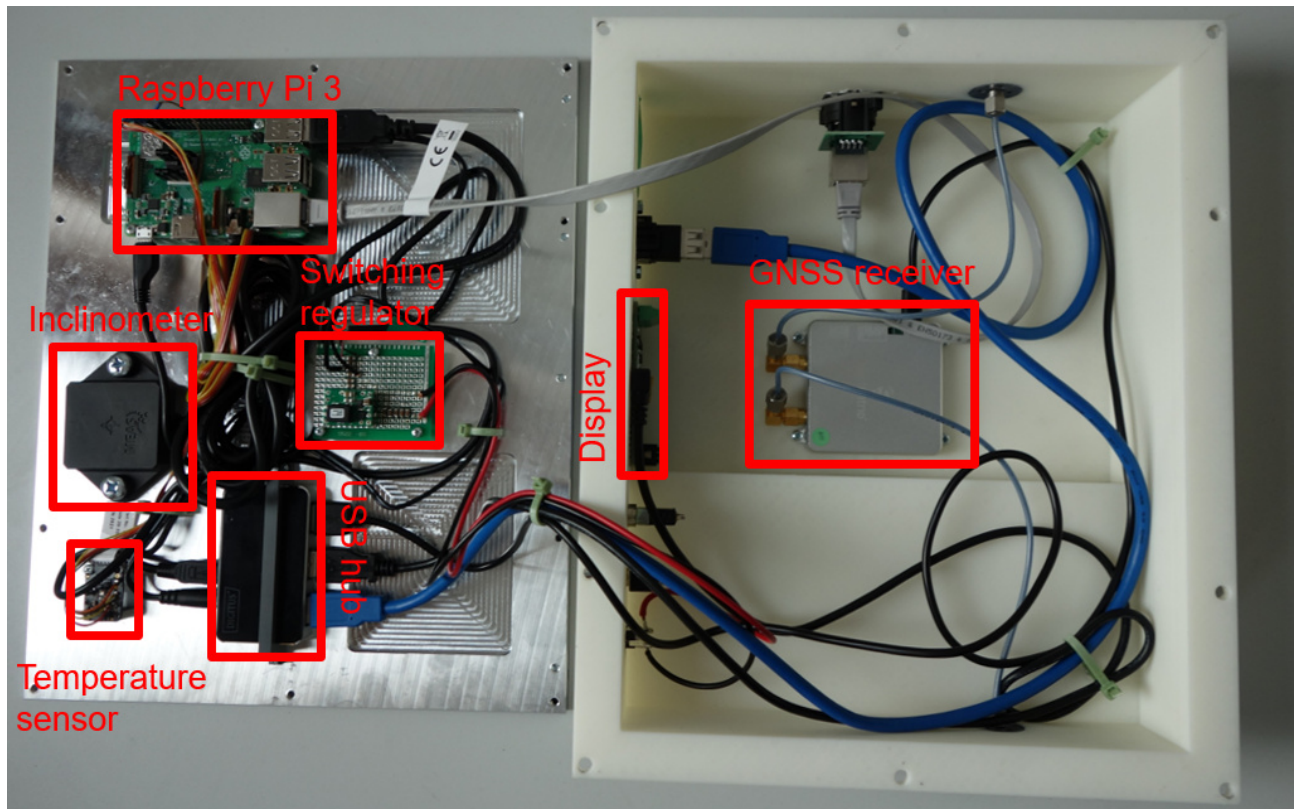


Figure 16: Realisation of the alignment measurement instrument



## 5 Validation of the Alignment Measurement Tool

The validation of the alignment measurement tool is done in several steps. At first the different errors influencing the accuracy of the instrument are analyzed and tried to be avoided, mitigated or compensated wherever possible. From the remaining errors, an uncertainty for the results can be predicted. After knowing the expected uncertainty of the alignment and position determination, the strategy for the validation of the measurement device is presented. Different validation methods are introduced, and a suitable validation method is selected. The validation is separated in a component validation in which the uncertainties of the individual components influencing the final alignment and positioning accuracy (such as the inclinometer, the GNSS receiver and the optimizer used for the determination of the transformation) are checked. An independent reference measurement is performed. The setup and results of this reference measurement is shown. These results are verified by a second independent measurement method to provide confidence and to justify that the alignment determined by the reference method is valid. Finally, the results and uncertainties of the alignment measurement instrument are provided and discussed, i. e. by comparing them with the reference measurement's values. All uncertainties provided in the following chapters are given as  $1\sigma$  standard deviation. If a different representation format of the uncertainty is used, it is noted.

### 5.1 Instrument Error Estimation

The goal for the measurement instrument is to improve on the previous used alignment method with magnetic compass and a digital inclinometer. At least the uncertainty of the magnetic compass of  $0.5^\circ$  shall be reached for the azimuth angle and the uncertainty of the inclinometer of  $0.2^\circ$  shall be achieved for the elevation angle. Before starting with the validation, the error influences on the measurement instrument are estimated and the uncertainty of the instrument is predicted.

The uncertainty of the measurement instrument is influenced by different error sources. The maximum achievable uncertainty is limited by the specified accuracies of the used sensors as well as the fitting error of the optimizer. The accuracy of the GNSS receiver used for the attitude angles depends on the baseline length, i. e. the distance of the measurement antennas. For an one meter baseline, an accuracy of  $0.15^\circ$  (heading) and of  $0.25^\circ$  (pitch / roll) is specified [31]. For a baseline of 5 meters an heading accuracy of  $0.03^\circ$  and pitch / roll accuracy of  $0.05^\circ$  can be expected. The measurement instrument is validated with 1.5 meter corner reflectors because it is the most common reflector at DLR's calibration test field. The outer edge length of the baseplate of this corner reflector amounts to  $1.5m \cdot \sqrt{2} \approx 2.12$  meters. By adding the length of the fixations which is  $2 \cdot 0.5$  meters, an entire baseline length of about three meters is reached. For this baseline length the accuracy of the GNSS receiver for the heading can be expected as  $0.05^\circ$  and  $0.08^\circ$

for the pitch / roll angle. When it comes to the position accuracy, the GNSS receiver provides a horizontal accuracy of 0.006 m and a vertical accuracy of 0.01 m. All these values are specified under the condition of an open sky. [31]

The inclinometer provides an accuracy of  $0.2^\circ$  at room temperature and an accuracy of  $0.6^\circ$  over the entire temperature range from  $-40^\circ\text{C}$  up to  $85^\circ\text{C}$ . It is assumed that the high deviations will be seen near the specified temperature limitations. The uncertainty for the inclinometer for the measurement instruments applicable temperature range ( $-10^\circ\text{C}$  up to  $70^\circ\text{C}$ ) will be determined in chapter 5.3.1. [32]

For the optimizer which fits an ideal corner reflector to the measurement's results it is aimed to reach an error below of 0.1 millimeters. Therefore, the influence of the optimizer for the positioning and the alignment angles can be neglected. The error of the optimizer with different error functions is presented and analyzed in chapter 5.3.1.

The inclinometer is placed on the baseplate of the corner reflector to measure the pitch and roll angle of the baseplate. When the baseplate is deformed in the area where the inclinometer is located, the measured angles are falsified. The same effect can be seen when the baseplate is covered in ice or plants such as moss. Even a small deformation such as one millimeter at the edge of a 1.5 meter reflector results in a change of the measured pitch angle of  $0.054^\circ$  which can be calculated with the following equation with  $\Delta d$  as the deformation and  $\vec{bp}$  as the vector of the baseplate pointing from the phase center to the edge of the corner reflector:

$$\Delta pitch = \arcsin\left(\frac{\Delta d}{|\vec{bp}|}\right) \quad (41)$$

To avoid this error, plants and ice is removed from the corner reflector's surface before the measurement instrument is mounted on the corner reflector. For the corner reflector which is used for the validation, the deformation is determined beforehand so that this error can be considered for the validation of the measurement instrument. The determination of the deformation of the used corner reflector is described and discussed in chapter 5.3.2.

Another possible source of error is the bending of the corner reflector's baseplate due to the weight of the measurement instrument itself which is placed on the baseplate. To avoid this error, the pitch angle of the baseplate is measured with a digital inclinometer before, after and when the measurement instrument is mounted. The difference in the angle is then compared to get the influence of the weight of the instrument on the accuracy of the alignment determination.

The accuracy is also impacted by the satellite visibility and the influence of multipath on the GNSS antennas. For the satellite visibility, a corner reflector on the calibration test field is selected where the visibility of the sky is not influenced by surrounding objects. Additionally, the visibility is improved by design by tilting the GNSS antennas by  $20^\circ$  to

allow even at large elevation angles a good visibility for both antennas. In regards to the multipath errors, antennas are selected which provide multipath rejection. The length of the fixation is chosen, so that the metal plates of the corner reflector do not influence the visibility and to reduce the multipath effect on the antennas.

The mechanical tolerances of the antenna's fixations influences the accuracy of the baseline length which is used for the automatic determination of the corner reflectors length and the calculation of the phase center position. To avoid this error, the fixations are measured up to one millimeter accuracy.

The susceptibility of the components to temperature as well as the long-term stability also influences the precision of the measurement. As discussed before, the accuracy of the inclinometer depends on temperature and is specified as  $0.6^\circ$  for the temperature range from  $-40^\circ\text{C}$  up to  $70^\circ\text{C}$ . The thermal introduced error on the inclinometer is determined as an uncertainty of  $\pm 0.2871^\circ$  for the roll angle and  $\pm 0.2351^\circ$  for the pitch angle ( $3\sigma$ ) in the temperature range from  $-10^\circ\text{C}$  up to  $70^\circ\text{C}$  from the single component validation from the upcoming chapter 5.3.1.

It is expected that the measurement instrument reaches a slightly higher uncertainty as the GNSS receiver and the inclinometer. Therefore, with respecting, as far as possible, all of the above described errors, the expected uncertainty of the alignment angles is  $\pm 0.15^\circ$  for the azimuth ( $3\sigma$ ) which is derived from the specified accuracy of the heading of the used GNSS receiver. The uncertainties for the roll angle of  $\pm 0.2871^\circ$  ( $3\sigma$ ) and for the elevation angle  $\pm 0.2351^\circ$  ( $3\sigma$ ) is calculated from the uncertainty of the inclinometer of  $0.2^\circ$  ( $3\sigma$ ) at  $25^\circ\text{C}$  and the thermal uncertainties of inclinometer 1 from table 3 in the upcoming chapter 5.3.1 ( $0.0687^\circ$  for roll and  $0.0412^\circ$  for elevation angle) with the following equation:

$$\sigma_{sys} = \sqrt{\sum_i \sigma_i^2} \quad (42)$$

The expected uncertainty of the position is estimated as  $\pm 0.006$  meters for the horizontal accuracy and as  $\pm 0.01$  meter for the vertical accuracy for the 1.5 meter corner reflector which are the specified accuracies of the used GNSS receiver. The three dimensional accuracy of the position can be calculated from the horizontal and vertical accuracy with the following equation and approximates as 0.0117 meter:

$$\sigma_{3D} \approx \sqrt{\sigma_{hor}^2 + \sigma_{ver}^2} \quad (43)$$

In the next section, different validation methods are discussed which can be used to provide a reference for the measurement instrument's measurement and to validate the

accuracy of the measurement instrument. The methods are compared, and a suitable strategy is selected.

## 5.2 Strategy of Validation

The strategy for the validation of the measurement instrument consists of a single component validation and an end-to-end validation. The single component validation verifies the performance of the individual components such as the inclinometer, the GNSS receiver, and the optimizer for the transformation of the virtual reference corner reflector model. These components provide the limits of the reachable uncertainty. Mainly the inclinometer which provides the worst uncertainty of  $0.6^\circ$  over temperature is analyzed in more detail. The least square optimizer is tested with different error functions in a theoretical simulation and a practical test. For the GNSS receiver, the tolerances of the attitude angles and the position are estimated by the receiver itself and provided in the datasheet. The determined tolerances are provided to the user as accuracy estimation for the current alignment via the web interface. These estimated tolerances are compared with the device validation's results.

In the device validation, the noise, repeatability and the deviation to the independent reference measurement is evaluated. Therefore, the instrument is mounted on the corner reflector and the alignment angles are determined as well as the corner reflector's phase center position. To validate these values, reliable reference measurements must be conducted. To validate the position, a precise GNSS receiver called GS16 from Leica is used. With this receiver a horizontal uncertainty of 8 millimeters and a vertical uncertainty of 15 millimeters can be reached for RTK measurements which is slightly worse than the uncertainties of the used GNSS receiver from Septentrio. [35]

As a reference measurement for the alignment angles of the corner reflector, a validation method would be to use a gyro compass for the determination of the azimuth angle and a digital inclinometer for the determination of the elevation angle. The elevation angle must be calculated from the measurement of the pitch angle of the baseplate by applying the bore sight offset of  $35.26^\circ$ . Unfortunately, the elevation angle measurement is largely influenced by the deformation of the corner reflector. This error must be compensated by measuring the deformation of the corner reflector and calculating the pitch offset. The available digital inclinometer at DLR provides an uncertainty of  $0.2^\circ$  and is therefore in the same range as the expected uncertainty of the measurement instrument's elevation angle measurement.

The gyro compass aligns with the meridian and allows the determination of the north south direction. The compass is not magnetic and therefore not influenced by magnetic materials nearby as well as it detects the true north's direction. In [36] a MEMS gyro compass is described which reaches a noise accuracy of 2 milliradians which is equivalent

to  $0.115^\circ$  with an averaging time of five minutes. Unfortunately, the compass is influenced by additional errors such as the mechanical tolerances of the fixation and the tilt of the instrument to the horizontal reducing the accuracy of the azimuth measurement. Additionally, the measurement is influenced by long-term bias drifts, turn-on to turn-on bias shift and bias variation over temperature which can be compensated by carousing. [36] The disadvantages of this measurement are the low accuracy due to mechanical errors of the fixation and the leveling error and its settling time of 5 minutes each time when changing the alignment or moving the gyro compass. Due to these disadvantages, different reference measurement methods are evaluated.

Another possible method for the reference measurement would be to align the corner reflector with the north star at a certain time which roughly points to the true north [37]. Due to the positioning of the north star near the celestial pole, it is moving in a small circle around the celestial pole over the night [37]. Therefore, the corner reflector can be aligned to the north star by using a telescope mounted on top of the corner reflector allowing to get the precise alignment of the reflector. When knowing the time at which the alignment is performed, the azimuth and elevation angle can be calculated for the stars position. To get the exact alignment of the reflector to the star, the telescope must be mounted exactly horizontally on the corner reflectors top. Therefore, a fixation with leveling sensors must be built. Additionally, the alignment can only be done at night and with a clear view at the sky. Due to the extended time effort for this measurement method, it is decided not to use this method for the validation of the measurement instrument.

A third method uses a tachymeter in order to measure the alignment. The tachymeter is oriented to north using a GNSS receiver allowing all points to be measured in global geodetic coordinates. The tachymeter then measures the points of the three vertices of the trihedral corner reflector using markers. From these three points a plane can be defined, and the normal vector can be calculated which points in the same direction as the bore sight of the corner reflector. With projections, the azimuth and elevation angle can be calculated as described in chapter 4.1.3. The tachymeter uses leveling bubbles and internal compensation mechanism to avoid leveling errors. An accuracy of two millimeter can be achieved with the tachymeter with a measurement time of two seconds [38]. The tachymeter offers an accurate and time efficient method to determine the alignment.

A fourth method would be to measure the whole surface of the corner reflector's planes with a tachymeter and to fit an ideal corner reflector model onto the measured model. The tachymeter is again oriented to north by a GNSS receiver. The attitude angles of the fitted model can be determined in the same way described with the third method by defining the plane from the three vertices as well as the normal vector and calculating the azimuth and elevation of the normal vector. It is superior over method 3 as the alignment is based on hundreds of measured points instead of only three corner vertices. Addition-

ally, this method allows the determination of the corner reflectors phase center position. This method is also suitable for the validation of the measurement instrument.

The third method using the tachymeter for measuring the three vertices of the reflector is selected as reference method for the device validation and the fourth method is used to verify the results of the third method in order to make sure that the reference measurement provides correct reference values for the alignment. In the following chapter the results of the validation are presented and discussed.

### **5.3 Results of the Validation**

In this chapter, the results of the validation are presented. First, the component validations setup and results are provided. The single component validation consists of the validation of the inclinometer's accuracy over temperature and the stability of the values over time. The GNSS receiver's estimated accuracy is trusted and therefore not additionally validated. The error influence of the optimizer for different optimizer error functions is checked with simulations and a practical test. The error function with the best results is selected for the measurement instrument's application. Afterwards, the setup and results of the reference measurements for the corner reflector are presented. The results of the alignment and position of the measurement instrument are compared to the reference measurements' values. The uncertainty and repeatability of the alignment and position measurement of the measurement instrument is checked and compared to the estimated uncertainties defined in chapter 5.1. Finally, the results are discussed.

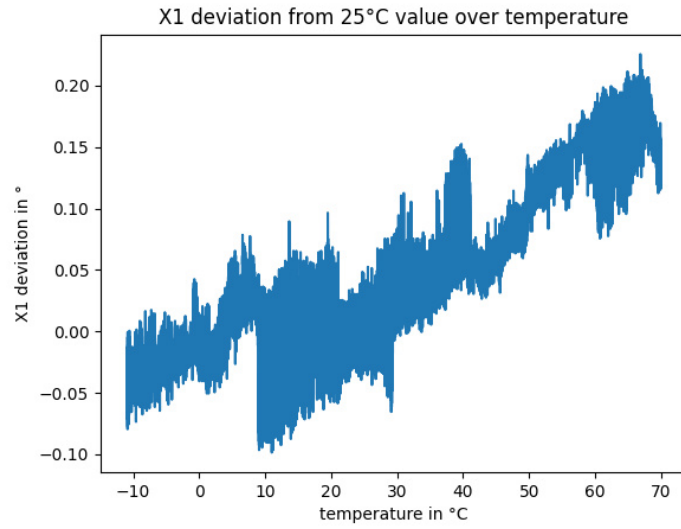
#### **5.3.1 Results of Single Component Validation**

During the single component validation, the main components influencing the uncertainty of the alignment and positioning of the developed measurement instrument are rechecked for their accuracy. These components are the inclinometer, the GNSS receiver and the optimizer.

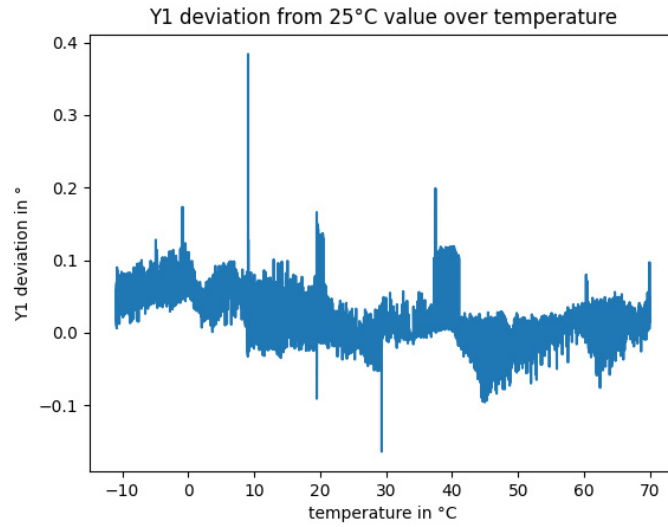
##### **Inclinometer Validation**

The inclinometer is checked due to its low accuracy of  $0.6^\circ$  over the specified temperature range from  $-40^\circ\text{C}$  up to  $85^\circ\text{C}$ . An operating temperature range of  $-10^\circ\text{C}$  up to  $70^\circ\text{C}$  is expected. The inclinometer's achievable accuracy is checked in a thermal test in which two 2-NSDOG2-021 inclinometers from TE Connectivity are validated. In this test the two inclinometers are mounted on a wooden plank to avoid a change of the angles due to thermal expansion of the mounting surface. The plank is placed inside a climate chamber and the pitch and roll angles are measured over temperature. A temperature sensor is placed near both inclinometers in order to get the exact temperature at the components. The measured data is evaluated relative to the mean pitch and roll value at  $25^\circ\text{C}$ . The

standard deviation for the thermal deviation is determined for the error estimation. For the first inclinometer the angle deviations from 25°C for the X and Y axis is displayed in figure 17



(a)

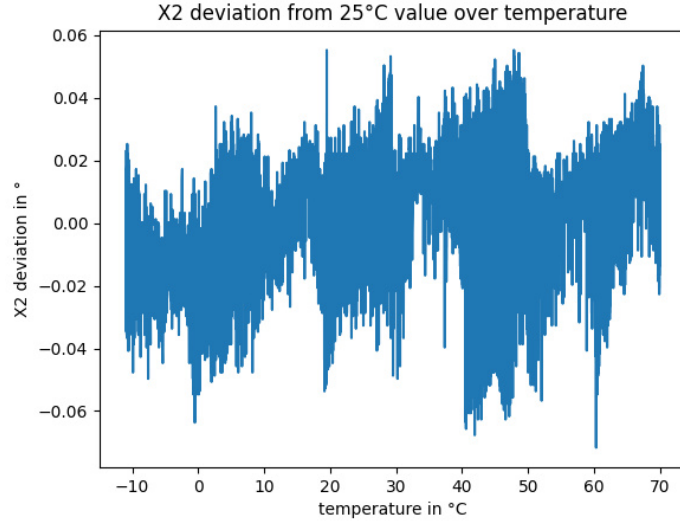


(b)

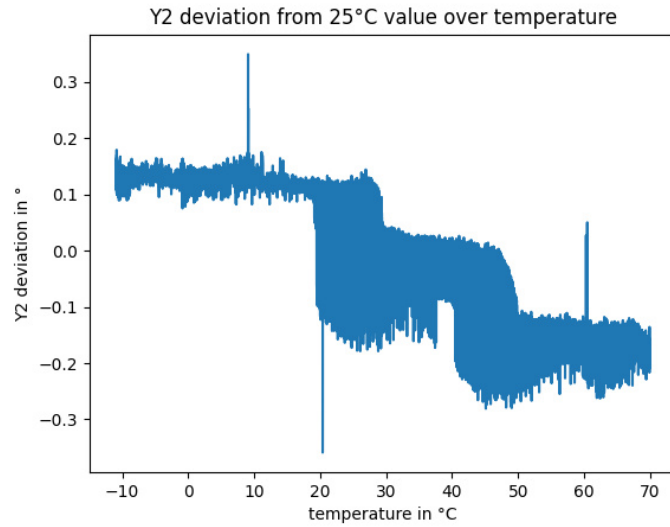
Figure 17: Inclinometer 1 deviation from 25°C value over temperature  
(a) x axis angle deviation over temperature  
(b) y axis angle deviation over temperature

It can be seen from the measurement results that the first inclinometer is sensitive to temperature changes. For the x-axis of the inclinometer the angle decreases by a maximum of 0.1° when the temperature is falling. At a rise of the temperature, the angle deviation is also increasing up to 0.22°. On the other hand, the y-axis seems to be a lot more stable. When neglecting the outliers at 9°C and 29°C which are not included in the  $3\sigma$  interval

the deviation is limited to an interval of  $+0.2^\circ$  to  $-0.1^\circ$ . In figure 18 the results for the validation of the second inclinometer over temperature is visualized.



(a)



(b)

Figure 18: Inclinometer 2 deviation from 25°C value over temperature  
(a) x axis angle deviation over temperature  
(b) y axis angle deviation over temperature

By evaluating the measurement it can be noticed that for the second inclinometer the x-axis is much more stable than the y-axis as well as both axis of the first inclinometer. The deviation is limited to an interval of  $+0.06^\circ$  to  $-0.075^\circ$ . Unfortunately, the y-axis of the second inclinometer performs much worse than both axis of the first inclinometer. With neglecting the outliers at 8°C and 20°C the y-axis deviation is inside the interval from  $0.17^\circ$  down to  $-0.28^\circ$ . In contradiction to the behavior of the first inclinometer, with



a decrease in temperature, the deviation rises and stays nearly at  $0.13^\circ$  for temperatures below  $18^\circ\text{C}$ . The good performance of the x-axis with a standard deviation of  $0.02^\circ$  and the worse performance of the y-axis of the second inclinometer with a standard deviation of  $0.126^\circ$  in comparison to the results of the first inclinometer can also be seen in the comparison of the standard deviations shown in table 3.

	X1	Y1	X2	Y2
$\sigma$ temp	$0.0687^\circ$	$0.0412^\circ$	$0.0203^\circ$	$0.1256^\circ$
$\sigma$ stability long time	$0.0087^\circ$	$0.0063^\circ$	$0.0084^\circ$	$0.0085^\circ$
$\sigma$ stability short time	$0.0083^\circ$	$0.0058^\circ$	$0.0077^\circ$	$0.0060^\circ$

Table 3: Standard deviation of inclinometer's axis angle deviation over temperature and during long and short time stability at room temperature

Additionally, the long time and short time stability of the inclinometers is checked in order to identify drifts over time. In these tests which are done at room temperature, all axis of the inclinometers perform similar which can be seen by comparing the standard deviations in table 3. The standard deviations of the stability tests are significantly smaller than the ones for the thermal deviations and therefore do not have an influence on the accuracy of the inclinometer and can be neglected.

Due to the large difference in the standard deviation of the thermal test between the x and y-axis for the second inclinometer, it is decided to use the first inclinometer for the measurement instrument because the angle deviations of both axes are quite similar to each other. The inclinometer is installed in the measurement instrument so that the x-axis is sensing the roll angle and the y-axis is sensing the pitch angle of the corner reflector's baseplate. A calibration can be added to compensate the temperature error for the inclinometer axis if needed. Therefore the thermal deviation must be evaluated whenever the inclinometer is changed and the compensation must be adapted. For now, the thermal error is considered in the error estimation of the instrument. With respecting the accuracy of the inclinometer of  $0.2^\circ$  ( $3\sigma$ ) at  $25^\circ\text{C}$ , the entire error over temperature for the applicable temperature range from  $-10^\circ\text{C}$  up to  $70^\circ\text{C}$  can be calculated from the thermal standard deviation with equation (42) from chapter 5.1 as  $0.0957^\circ$  (equals  $0.287^\circ$  as  $3\sigma$  value) for the roll angle and as  $0.0783^\circ$  (equals  $0.235^\circ$  as  $3\sigma$  value) for the pitch angle. An overview of the accuracies achievable with the selected inclinometer is shown in table 4.

## GNSS Receiver Validation

For the GNSS receiver the estimated accuracy of the heading angle of the receiver as well as the position accuracy estimation done by the receiver is trusted. These estimated standard

	roll angle	pitch angle
$\sigma$ temp	0.0687°	0.0412°
$\sigma$ at 25°	0.0666°	0.0666°
$\sigma_{combined}$	0.0957°	0.0783°
$3\sigma_{combined}$	0.287°	0.235°

Table 4: Overview of uncertainties for pitch and roll angle of the selected inclinometer 1

deviations are used for the internal error estimation of the measurement instrument and are displayed for the user on the web interface as  $3\sigma$  tolerance.

### Optimizer Validation

Another component that has a large influence on the accuracy of the alignment angles and the phase center position of the corner reflector is the optimizer for the transformation of the reference corner reflector model in the ENU frame from which the alignment and the phase center position is calculated. Different algorithms are tested in a theoretical simulation as well as in the practical application. The results of each algorithm for the error function of the optimizer are compared and the algorithm with the best result is selected.

For the theoretical simulation, a virtual corner reflector model is created in the reference frame as described in chapter 4.1.3. The model is defined by the coordinates of the vertices of the reflector and the GNSS antennas positions on the reflector. As origin for the coordinate system, a reference point is defined on the corner reflector which is located in the middle of the front edge of the baseplate. The virtual reflector model is rotated with the Euler convention around a certain roll, pitch and heading angle. A translation is performed for all points so that the main GNSS antenna is the origin of the transformed coordinate system which resembles the position of the main antenna in the ENU coordinate frame. This represents the aligned corner reflector for which the unknown transformation from the reference frame shall be determined to the measured points by the optimizer. The reference frame is the coordinate frame in which the virtual corner reflector model is defined and the phase center position is known. The ENU coordinate frame is the coordinate system in which the GNSS antenna's positions are known but the position of the corner reflector's phase center is unknown. Therefore, the transformation from the reference frame with the known phase center position to the ENU frame must be determined in order to get the position of the phase center in the ENU frame.

In the real application only the main and auxiliary antenna's positions are known in the ENU coordinate system. These positions from the test corner reflector are used as input for the optimizer. The optimizer tries to fit the transformation parameters which consists of three rotation angles as well as three translations in x, y and z direction to minimize the error between the real antenna positions and the transformed ones from the

reference frame. As starting values for the transformation the heading, pitch and roll as well as the main antenna's coordinates of the reference reflector model are used. With the optimization, only the antennas baseline can be fitted correctly. The phase center position is still ambiguous due to not knowing the pitch angle of the baseplate. In order to fix this ambiguity, different algorithms are tested which include the pitch information in the optimizer's error function and whose functionality and results are provided hereinafter. After the transformation is done, the error of the optimizer is determined by calculating the deviation between the test corner reflector's phase center position and the phase center position of the corner reflector estimated by the optimizer. This position is evaluated for the x, y and z deviation for heading angles ranging from  $0^\circ$  to  $360^\circ$  with a step size of  $10^\circ$  and pitch and roll angles in the range of  $-90^\circ$  to  $90^\circ$ , both angles with a step size of  $5^\circ$  in order to achieve a realistic simulation duration.

**Optimizer 1:** For the first algorithm, reference angles must be determined which are compared with the attitude angles of the transformed reflector model. The reflector model's baseplate is rotated by the measured roll and pitch angle. For the rotated baseplate, the pitch and roll angle to the x-y coordinate plane is determined. These two angles describe the orientation of the baseplate for the measured alignment and are called reference angles. The reference reflector model is transformed with the initial values of the optimizer. For this transformed model, the pitch and roll angle of the baseplate is determined to the x-y coordinate plane. The difference between these angles and the reference angles is calculated and returned as error additional to the antennas coordinates deviations to the optimizer. The optimizer calculates the costs from these errors, adapts the parameters for the transformation and repeats the transformation with the new parameters. This cycle is repeated until the error is minimized. The minimization process described above can be expressed simplified with the following equation with  $P_{meas}$  as measured coordinates of the main and auxiliary antenna,  $P_{model}$  as the transformed coordinates of the main and auxiliary antenna from the reflector model,  $roll_{xy,ref}$  and  $pitch_{xy,ref}$  as the reference angles and  $roll_{xy,model}$  and  $pitch_{xy,model}$  as baseplate pitch and roll angle to the x-y plane for the transformed model:

$$\min (||P_{meas} - P_{model}|| + ||roll_{xy,ref} - roll_{xy,model}|| + ||pitch_{xy,ref} - pitch_{xy,model}||) \quad (44)$$

For calculating the angles with respect to the x-y plane, the projections described in chapter 4.1.3 are used. The error of the phase center position in x, y and z with respect to the attitude angles is displayed in figure 19.

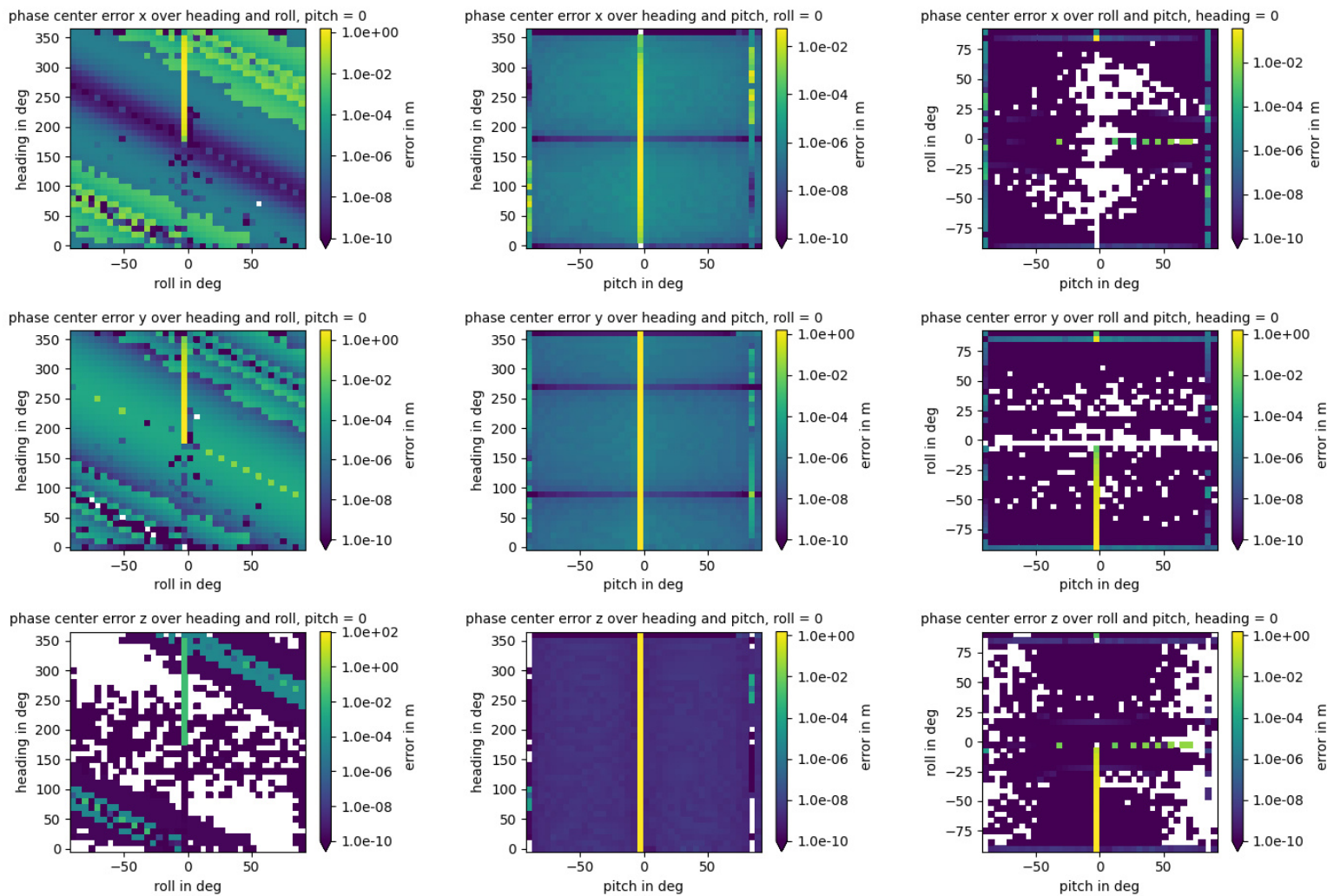


Figure 19: Simulation results for the algorithm comparing the pitch and roll angle

A deviation can be seen above the desired deviation of 0.1 millimeters at a few alignments with a pitch angle equal to zero,. The largest deviation over 'heading and roll' of about one meter can be seen for heading angles above of 180° and roll angles below 0°. White spots in the plots mean that there is no error between the transformed and test phase center coordinate. For the deviation over 'heading and pitch' it can be seen that the error is neglectable (below  $10^{-5}$ ) except for pitch values near 0° where the deviation is increasing up to one meter. For the deviation over the 'pitch and the roll angle' the same behavior can be seen for pitch angles near 0° and a roll angle smaller than 0°. For pitch angles near zero degree the error increases because the angle cannot or hardly be determined by the algorithm due to the fact that there is no cutting angle between the baseplate and the x-y plane (co-planar). For pitch angles near zero the desired deviation of 0.1 millimeters cannot be reached. This is a disadvantage of this method.

**Optimizer 2:** Another method which avoids the disadvantage of the previous method is to determine and compare the pitch angle of the baseplate to all three coordinate planes additional to comparing the antenna's coordinates. If the baseplate is co-planar to the x-y plane and has no cutting angle with this plane, there is at least one other coordinate plane (x-z or y-z) to which a cutting angle exists for the baseplate. For this algorithm, the baseplate of the reference model is rotated by the measured roll, pitch and heading angle. The pitch angle of this rotated baseplate is calculated to all three coordinate planes. The resulting three angles are used in this method as reference angles for the comparison with the transformed model. The reference model is transformed with the initial parameters of the optimizer and the pitch angles to the three coordinate planes are calculated for the transformed model's baseplate. The projections described in chapter 4.1.3 are used to calculate the angles to all three coordinate planes. The difference between the calculated angles and reference angles is returned as error to the optimizer. Additionally, the deviation of the coordinates of the transformed main and auxiliary antennas positions to the measured antenna positions are returned as error to the optimizer. The optimizer determines the costs and adapts it's parameters until the costs are minimized. The optimization process described above can be expressed simplified with the following equation with  $P_{meas}$  as measured coordinates of the main and auxiliary antenna,  $P_{model}$  as the transformed coordinates of the main and auxiliary antenna from the reflector model,  $pitch_{xy,ref}$ ,  $pitch_{yz,ref}$  and  $pitch_{xz,ref}$  as the reference angles and  $pitch_{xy,model}$ ,  $pitch_{yz,model}$  and  $pitch_{xz,model}$  as baseplate pitch angles to all three coordinate planes for the transformed model:

$$\begin{aligned} \min(&||P_{meas} - P_{model}|| + ||pitch_{xy,ref} - pitch_{xy,model}|| + ||pitch_{yz,ref} - pitch_{yz,model}|| \\ &+ ||pitch_{xz,ref} - pitch_{xz,model}||) \end{aligned} \quad (45)$$

The error of the phase center position for this error function is displayed in x, y and z for the described range of the attitude angles in figure 20.

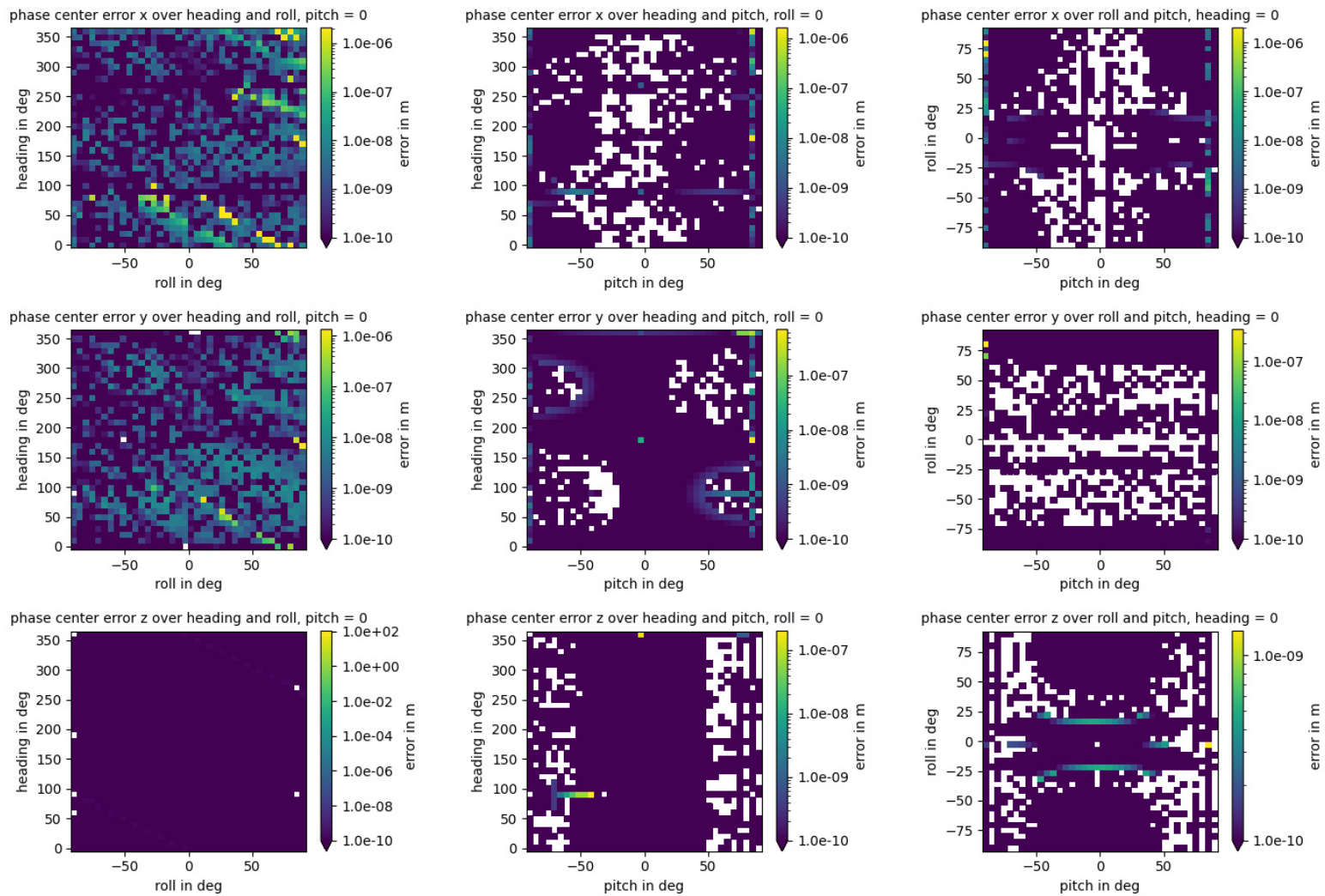


Figure 20: Simulation results for the algorithm comparing the pitch angle to all three coordinate planes

It can be seen that the algorithm provides good results with a maximum error of  $2 \cdot 10^{-5}$  meters which is below the desired deviation of 0.1 millimeters. White spots in the graphics indicate that there is no difference between the test phase center and the phase center determined with the transformation. Therefore, the algorithm is suitable for the optimizer.

**Optimizer 3:** As a third algorithm, the pitch angle of the baseplate to the x-y plane is compared additionally to the antennas coordinates. The baseplate of the reference reflector model is rotated by the measured pitch and roll angle and the pitch angle to the x-y plane is calculated for the rotated baseplate. This angle is the reference angle. The corner reflector model is transformed with the initial parameters of the optimizer. The pitch angle to the x-y plane is calculated for the baseplate of the transformed model. This calculated pitch angle is compared with the reference pitch angle and the error is returned together with the antennas coordinates deviations to the optimizer. The optimizer calculates the costs, adapts its parameters and repeats the cycle until the costs are minimized. The optimization process described above can be expressed simplified with the following equation with  $P_{meas}$  as measured coordinates of the main and auxiliary antenna,  $P_{model}$  as the transformed coordinates of the main and auxiliary antenna from the reflector model,  $pitch_{xy,ref}$  as the reference pitch angle to the x-y plane and  $pitch_{xy,model}$  as the baseplate pitch angles to the x-y plane of the transformed model:

$$\min(||P_{meas} - P_{model}|| + ||pitch_{xy,ref} - pitch_{xy,model}||) \quad (46)$$

The remaining error of the phase center position for this algorithm is shown in figure 21.



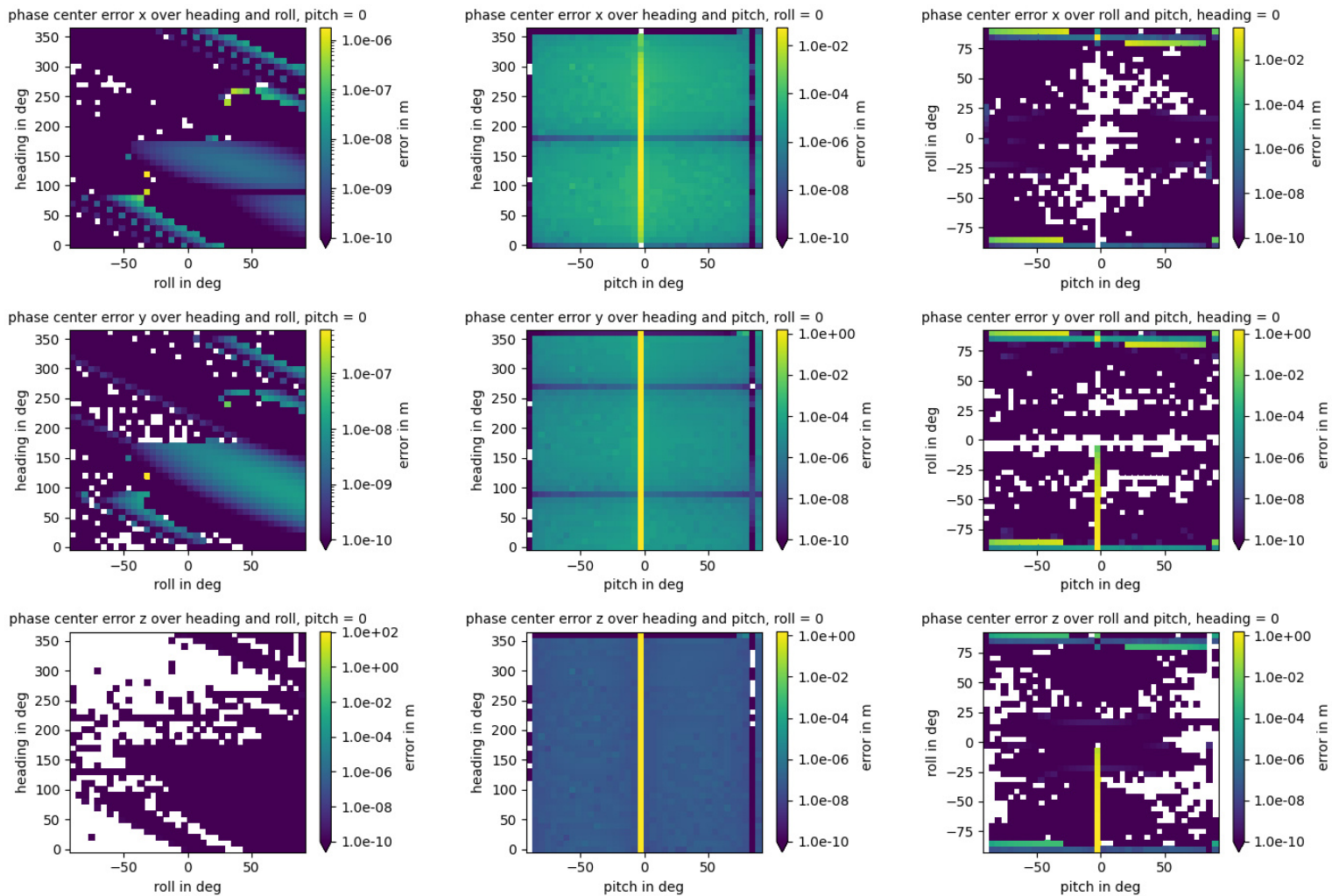


Figure 21: Simulation results for the algorithm comparing the pitch angle of the baseplate determined with projection to the z-axis

It can be seen from the results that for the deviation over 'heading and roll' with a pitch angle equal to zero the error is comparable to the previous algorithm with an maximum deviation of  $2 \cdot 10^{-6}$  meters and within the desired limits. For other alignment angles, the algorithm is not performing well. For the deviation over 'heading and pitch', the error stays mostly in the range of 0.1 millimeters except for pitch angles near  $0^\circ$  where the error increases up to one meter. For the deviation over 'pitch and roll', the error is neglectable low except for pitch angles near  $0^\circ$  and roll angles below  $0^\circ$  as well as for roll angles close to  $\pm 90^\circ$  where the error increases up to one meter. Even though the algorithm does not perform well for some alignments, this algorithm is checked in a practical test together with the other ones.

The three different optimizer error functions and the simulation results are compared in table 5.

algorithm	compared base-plate angles	max phase center error (pitch = 0)	max phase center error (roll = 0)	max phase center error (heading = 0)
optimizer 1	roll xy, pitch xy	1 m	1 m	1 m
optimizer 2	pitch xy, pitch yz, pitch xz	$2 \cdot 10^{-6}$ m	$1.5 \cdot 10^{-6}$ m	$2 \cdot 10^{-6}$ m
optimizer 3	pitch xy	$1.5 \cdot 10^{-6}$ m	1 m	1 m

Table 5: Overview of optimizer error function algorithms and simulation results

For the practical test, the different error function algorithms for the optimizer are implemented on the measurement instrument. The measurement instrument is then mounted to a 0.7-meter corner reflector with a pitch and roll angle close to  $0^\circ$ . The baseplate of the corner reflector is aligned with a pitch angle of about  $-0.79^\circ$ , a roll angle of about  $-1^\circ$  and a heading angle of about  $224^\circ$ . The alignment is measured with the measurement instrument and the transformation error as well as the positioning error of the main and auxiliary antenna and the pitch angle to the x-y plane is evaluated. The transformation error which is the final costs of the optimizer is calculated with the following equation from [39] with the usage of the 'huber' loss function  $\rho(x)$ ,  $f_i$  as the error function algorithm and  $x_{final}$  as the final transformation parameters:

$$err_{opt} = 0.5 \cdot \sum_i^m \rho(f_i(x_{final})^2) \quad (47)$$

with  $\rho(x)$  defined as:

$$\rho(x) = \begin{cases} x & \text{for } x \leq 1 \\ 2 \cdot \sqrt{x} - 1 & \text{for } x > 1 \end{cases} \quad (48)$$

The lower the final cost, the better is the fitting of the optimizer. It is assumed that for the phase center position a similar deviation can be achieved as for the positioning of the main and auxiliary antenna. The pitch angle to the x-y plane is used in every error function. The pitch angle error to the x-y plane returned by the optimizer can be used as an additional indicator how good the phase center position is fitted.

The transformation error as well as the deviations of the main and auxiliary antenna's positions and the deviation to the reference angle of the pitch angle determined to the x-y plane can be seen for the different algorithms in the following table 6.

error function algorithm	optimizer 1	optimizer 2	optimizer 3
transformation error	$1.3 \cdot 10^{-4}$	1.70	$7.65 \cdot 10^{-32}$
main antenna error east in m	-0.00453	0.00401	$7.40 \cdot 10^{-17}$
main antenna error north in m	-0.00472	1.1722	$-2.22 \cdot 10^{-16}$
main antenna error up in m	0.00931	-0.1022	$-5.78 \cdot 10^{-19}$
aux antenna error east in m	0.00453	-0.00401	$-2.22 \cdot 10^{-16}$
aux antenna error north in m	0.00472	-1.5166	$7.40 \cdot 10^{-17}$
aux antenna error up in m	-0.00931	0.1022	$1.15 \cdot 10^{-18}$
pitch xy angle error in °	$-2.14 \cdot 10^{-11}$	0.00296	$-5.55 \cdot 10^{-17}$

Table 6: Transformation error and antenna position and baseplate pitch angle to x-y plane deviation of the different error function algorithms in the practical test

As can be seen from the table, the algorithm 'optimizer 2' that performs the best during the theoretical simulation performs worst in the practical test with a transformation error of 1.7 and deviations up to 1.17 m. A reason for this behavior could be that the algorithm is sensitive to noise on the measured alignment angles. The algorithm 'optimizer 1' provides also worse results with positioning errors in the range of millimeters in the practical test. Surprisingly the algorithm 'optimizer 3' that performed not that well during the theoretical simulation shows very good results in the practical test with a transformation error of  $10^{-32}$  and positioning errors in the range of  $10^{-16}$ . For the deviation between the practical test and the simulation, no explanation can be provided which explains these major deviations.

Due to the extremely good results of the algorithm 'optimizer 3', it is used for the error function of the optimizer in the measurement instrument. Even though the effects of the optimizer error can be neglected, the fitting error determined by the optimizer for the main antenna is used for the error estimation of the measurement instrument. Together with the horizontal and vertical accuracy determined by the GNSS receiver the estimated uncertainty of the phase center's position can be calculated. Therefore, it is expected for the instrument to reach the accuracy estimated by the GNSS receiver during the validation measurement.

### 5.3.2 Results of Instrument Validation and Discussion of the Results

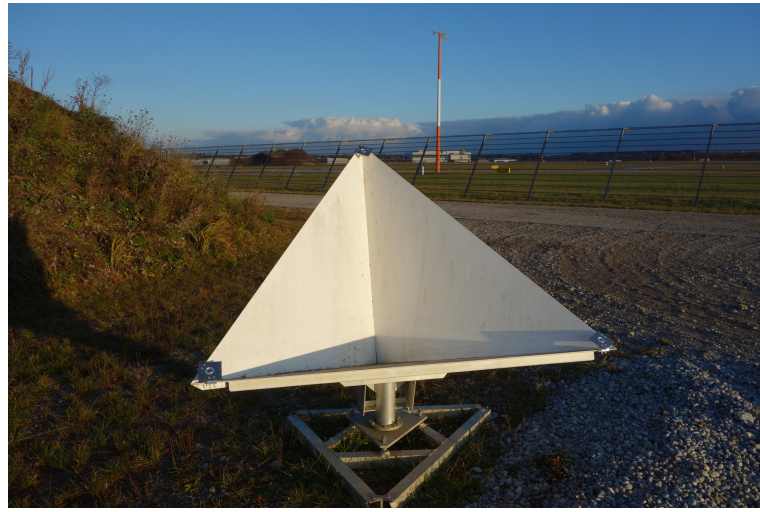
In this chapter, the results of the instrument validation are presented and discussed. The measurement setup is explained for each measurement. Firstly, the setup and results of the measurement methods selected in chapter 5.2 as reference methods is explained. These methods are used to provide the alignment of the corner reflector with a higher precision as the measurement instrument. The alignment determined by these reference measurements is assumed as the 'true' alignment of the corner reflector in order to determine the deviation of the measurement instrument's measurements to the actual alignment. Afterwards the reference alignment angles and the predicted uncertainties from chapter 5.1 are compared to the results of the measurement instrument and the results are discussed. The same comparison is performed for the validation of the phase center position. The reference for the position is determined by a commercial GNSS receiver (Leica GS16) with a high precision.

#### Reference Measurements

For the first reference measurement, the tachymeter TS16 from Leica Geosystems is used. It provides an accuracy for the measured distances of two millimeters [38]. The tachymeter is oriented to north with the GNSS receiver GS16 from Leica. The GS16 receiver is placed on a pole with a prism. The tachymeter is aligned to the prism mounted on the GNSS receiver and the position of the GNSS receiver is measured with the tachymeter. By knowing at least three points and their relative position to the tachymeter, the position of the tachymeter as well as the orientation of the tachymeter can be triangulated. With the tachymeter oriented, all points measured with the tachymeter can be given in ETRF/ITRF coordinates. The oriented tachymeter can be pointed to markers which are placed on the edges near the vertices of the corner reflector. A corner reflector with a low elevation angle is selected to avoid uncertainties by the tilted markers. The width of the laserbeam of the tachymeter which is used to measure the positions is not infinitesimal small. When hitting a plate that is not orthogonal to the laserbeam, the position can variate due to not knowing at which position inside the beam is measured. This is an additional error source. The three dimensional uncertainty of the measured points is estimated by the tachymeter as 3 millimeters. From the coordinates of the three vertices a plane is calculate as well as the normal vector on the plane. As described in chapter 4.1.3, the normal vector's direction is equal to the direction of the bore sight of the corner reflector whose alignment angles can be calculated with projections. The described measurement setup is displayed in figure 22.



(a)



(b)

Figure 22: Reference measurement setup

(a) tachymeter with GNSS receiver for position determination

(b) markers on corner reflectors corners

To verify the described reference measurement and to avoid error due to (potentially) bended corner reflector edges, the tachymeter is placed close to the corner reflector and measures points on the surface of the corner reflector. The tachymeter's position is determined with the GNSS receiver in the same way as described in the reference measurement. The angular resolution for the measurement is selected as  $1.5^\circ$ . With all the points on the corner reflector's surface measured, an ideal trihedral corner reflector can be fitted to the data. After fitting, the deformation of the reflector can be determined from the deviation from the ideal reflector. From this ideal corner reflector the alignment can be determined. This method is superior to the first reference because the alignment is determined based on almost 1000 points instead of only three points which can easily be influenced by errors such as measurement noise. Due to that, the alignment determined with the surface mea-

surement is much more stable.

In order to provide a better resolution of the deformation and to check the influence of the deformation on the measurement results, the deformation of the corner reflector is measured additionally with a laser scanner which does not support global positioning and the deviation is calculated from the laser scanner's data. The determined deformation for the corner reflector used for verification of the reference measurement and the validation of the measurement instrument is visualized in figure 23. The calculation of the alignment from the deformation measurements and the evaluation of the measured surface scans are provided by the calibration department of DLR and are therefore not described in detail in this thesis.

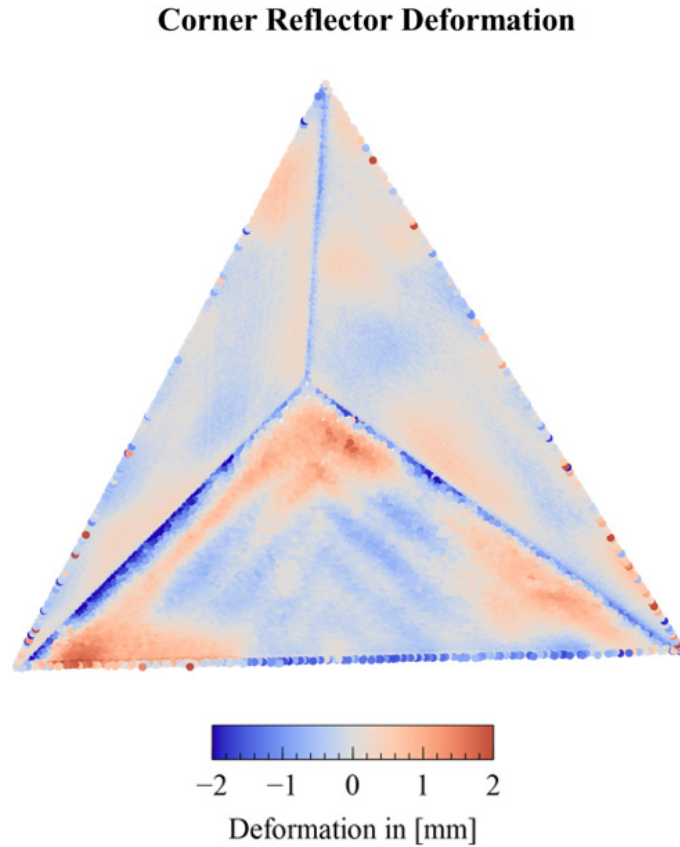


Figure 23: Deformation of the corner reflector used for the validation; corner size: 1.5 m

It can be seen that the baseplate is deformed near the phase center of the corner reflector. This deformation is caused by the stand of the corner reflector pressing on the baseplate. Additional deformations can be seen near the edges. The markers are placed at these edges so the positions measured by the tachymeter can be falsified by the deformation. For the left corner the deformation can be determined to about 1.5 millimeter. With the deformation calculations from chapter 5.1 the influence on the elevation angle can be calculated as  $0.081^\circ$  for the 1.5 m corner reflector. In the middle of the corner reflectors baseplate no or very small deformations can be seen. In this area, the inclinometer of

the measurement instrument is placed. Therefore, the measurement of the pitch and roll angle of the baseplate by the inclinometer is only neglectable influenced by deformations for this corner reflector.

The elevation and azimuth angle determined by the reference and the verification measurement can be seen in table 7.

angle	reference mea- surement	verification mea- surement	deviation
azimuth	261.64°	261.63°	0.01°
elevation	53.88°	53.81°	0.07°

Table 7: Alignment angle comparison between both reference measurement methods

It can be seen that the deviation between the azimuth angles is neglectable low and could be caused by tolerances of the measurements. The deviation for the elevation angle is largest with about 0.07° deviation which could be attributed to the deformation of the corner reflector near the vertices: The angle deviation for elevation is in the same range as the estimated error of 0.081° for a deformation of 1.5 millimeter of the baseplate at the left corner seen in figure 23.

The verification measurement shows that the determined alignment can be trusted and the causes for the deviations between the reference and the verification measurement can be explained. The deformation of the corner reflector near the edges are distorting the reference measurement. The alignment angles determined by this verification method are used as reference for the measurement instrument's alignment angles because the alignment measurement of the verification method is based on hundreds of points. In the following the results of the measurement instrument are presented.

### Alignment Angles Validation

The measurement instrument is placed on the corner reflector as described in chapter 4.1.1. The internal database is used to store the alignment and positioning values for the evaluation. For the alignment, the two possible methods, the alignment calculation through offsets from the reflectors geometry and through projection, explained in chapter 4.1.3, are analyzed and the results are compared. In figure 24, the setup for the validation measurements with the developed measurement instrument is shown.





Figure 24: Measurement setup for the validation of the measurement instrument

In regards to the alignment's uncertainty the noise of the measurement as well as the repeatability is determined. In order to evaluate these values, a measurement series is recorded. The measurement instrument is completely dismounted and mounted again and the next measurement series is started. Ten measurement series with at least 100 values for each series are performed. From these measurement series the ensemble mean, the sample standard deviation and the ensemble standard deviation is calculated. The ensemble mean is calculated as the mean value over all measurements ( $mean(mean(x_i))$ ). The sample standard deviation which is an indicator for the noise of the alignment measurement is calculated as the mean value of the standard deviations of each of the ten measurement series ( $mean(std(x_i))$ ). The ensemble standard deviation which is an indicator for the repeatability of the measurement is calculated as the standard deviation of the mean value of each measurement series ( $std(mean(x_i))$ ). Additionally, the deviation to the reference alignment angles presented above is calculated. In table 8 the results of the evaluation of the alignment measurements are shown for the offset method and in table 9 the results for the attitude angles of the projection method are presented.

When comparing the results of both measurement methods, it can be seen that the elevation angle value and the deviations are almost identical for both methods. On the other hand for the azimuth angle, the difference between the two methods is more significant. The azimuth deviates by  $0.04^\circ$  between both methods. The noise for the azimuth angle determined with the projection method ( $0.154^\circ$ ) is much higher than the one for the offset method ( $0.03^\circ$ ). An explanation for this could be, that for the offset method the



angle	ensemble mean	sample standard deviation (noise)	ensemble standard deviation (repeatability)	deviation from reference
azimuth	261.50°	0.033°	0.059°	0.13°
elevation	53.57°	0.006°	0.018°	0.24°

Table 8: Results of the offset method's alignment measurement of the measurement instrument with noise and repeatability measure and reference bias.

angle	ensemble mean	sample standard deviation (noise)	ensemble standard deviation (repeatability)	deviation from reference
azimuth	261.54°	0.154°	0.090°	0.09°
elevation	53.57°	0.006°	0.018°	0.24°

Table 9: Results of projection method's alignment measurement of the measurement instrument with noise and repeatability measure and reference bias.

azimuth angle is only influenced by the noise of the heading angle measured by the GNSS receiver. On the other hand, the azimuth angle determined with the projection method is influenced by the noise of the heading angle, the noise of the baseline length, the transformation error and the noise of the antennas position's measured by the GNSS receiver. Due to the good algorithm for the optimizer from chapter 5.3.1, the transformation error can be neglected.

For the azimuth angle determined with the offset method, it can be seen that the deviation due to noise of 0.03° and the deviation of the ensemble of 0.06° representing the repeatability of the measurement lie approximately in the range of the accuracy of the GNSS receiver of 0.05° for a 3 meter baseline. Also the deviation from the reference measurement of 0.13° lies inside the  $3\sigma$  interval of the GNSS receiver of 0.15° for a 3 meter baseline. For the projection method the results are worse. On the other hand, the deviation of the azimuth angle of the projection method to the reference measurement (0.09°) is smaller than the deviation of the offset method (0.13°). Both methods have their advantages and disadvantages for the determination of the azimuth angle.

As for the elevation angles, both methods provide the same results and can therefore be used for the measurement instruments elevation angle calculation. When comparing the standard deviation of the noise of 0.006° and of the repeatability of 0.018° of the elevation angle measurement with the determined accuracy of the inclinometer from table 4 of 0.0783° including the temperature uncertainty, it can be seen that the measurement instrument's measurement performs much better. As for the deviation from the reference elevation angle value the deviation of 0.24° is barely outside of the interval of 0.235° from table 4.

Overall for the alignment validation can be said that for the offset method and the elevation angle determined with the projection method the results are plausible and even reach

the accuracies of the used sensors which is a good result for the precision and accuracy of the measurement instrument. The estimated uncertainties in chapter 5.1 agree with the validation results. The projection method's azimuth angle is more influenced by noise than the offset method, but is overall closer to the reference method's angle than the offset method. The offset method can be used for the calculation of the azimuth angle, when a stabilized azimuth angle is desired. The deviation of the alignment angles with respect to the reference value lies inside of the tolerance of the GNSS receiver in case of the azimuth angle or is barely outside of the determined tolerance of the inclinometer in case of the elevation angle. These are also good results for the accuracy of the attitude determined with the measurement instrument.

### Phase Center Position Validation

The position of the phase center is calculated by the measurement instrument from the corner reflector's model fitted into the ENU frame by the optimizer. The position is therefore dependent on the positioning error of the GNSS receiver as well as the transformation error. With neglect of the transformation errors justified in chapter 5.3.1 the estimated accuracy of the GNSS receiver shall be reached. This accuracy is stated by the GNSS receiver as horizontal and vertical accuracy of the position. These accuracies are compared with the standard deviation and repeatability of the validation measurement. As reference measurement, the position of the corner reflector's phase center is measured with the tachymeter (see reference measurements). The Leica GS16 reference receives it's correction data from the SAPOS NTRIP caster which operates in the ETRS89/DREF91 reference system [20]. The GNSS receiver in the measurement device retrieves it's correction data from the same NTRIP caster and therefore works in the ETRS89/DREF91 reference system as well. No additional conversion between different reference systems is needed and the positions from both GNSS receivers can directly be compared. The coordinates of the corner reflector's phase center measured with the Leica GS16 which is used as reference are given in table 10.

coordinate	ETRS89/DREF91
latitude	48.0832645659183°
longitude	11.2791439517617°
height	626.904 m

Table 10: Reference measurement of corner reflector's phase center in the ETRS89/DREF91 reference coordinate frame

Similar to the alignment validation, multiple measurement series are done for the corner reflector's phase center position. A measurement series of the position is conducted, the measurement instrument is removed from the corner reflector and mounted again and the next measurement series is recorded. The mean value of the ensemble, the standard

deviation of a series (noise), the standard deviation of the ensemble which resembles the repeatability of the measurement and the deviation to the reference measurement of the position is calculated. These values are calculated in the same way as for the alignment angles. Additionally, for better interpretability of the results, the three dimensional position deviation is approximated in meters. Therefore, the geodetic standard deviations are added to the mean geodetic position coordinates. The resulting position is transformed into ENU coordinates and the difference to the mean ENU position is calculated in order to determine the standard deviation in meters. This approximation can be described with the following equation as well in which  $P_{geo}$  and  $\sigma_{geo}$  represent the position and the standard deviation in geodetic coordinates,  $P_{ENU}$  represents the position in the ENU coordinate system,  $T_{geo,ENU}$  the transformation from the geodetic coordinate frame to the ENU frame and  $\sigma_{ENU}$  the approximated three dimensional standard deviation in meters in the ENU frame.

$$\sigma_{ENU} \approx T_{geo,ENU}\{P_{geo} + \sigma_{geo}\} - P_{ENU} \quad (49)$$

In case of the deviation from the reference measurement, both positions are transformed into cartesian coordinates and the three dimensional deviation is calculated in meters. These results of the measurement instrument are presented in table 11.

coordinate	ensemble mean	standard deviation (noise)	ensemble standard deviation (repeatability)	deviation from reference
latitude [°]	48.0832646957	$4,066 \cdot 10^{-8}$	$2.5168 \cdot 10^{-8}$	$-1.298 \cdot 10^{-7}$
longitude [°]	11.2791441595	$4.17 \cdot 10^{-8}$	$8.7861 \cdot 10^{-8}$	$-2.1 \cdot 10^{-7}$
height [m]	626.9261	0.0055	0.0060	-0.022
3D deviation (approx) [m]	-	0.0082	0.0093	0.030

Table 11: Results of phase center position measurement determined by the measurement instrument

When comparing the 3D noise standard deviation of 0.0246 meter ( $3\sigma$ ) and repeatability of 0.0279 meter ( $3\sigma$ ) with the estimated three dimensional uncertainty of 0.0117 meter for the Septentrio receiver from chapter 5.1, it can be seen that the position accuracy is worse than the achievable accuracy of the GNSS receiver. However, when comparing the results with the estimated accuracy of 0.015 meter horizontally and 0.03 meter vertically ( $3\sigma$  values) of the receiver during the measurement which can be approximated with a three dimensional accuracy of 0.0335 meters, the results are much more realistic and can be justified by the receiver's estimation. By comparing the 3D deviations with the reference measurement, it can be seen that there is a deviation of about 0.03 meters between the

two position measurements which is included in the tolerance of the estimated measurement accuracy of the Septentrio GNSS receiver.

Overall, it can be said for the position, that the uncertainty due to noise and the repeatability uncertainty of the position is in the range of three centimeters in the validation results which is worse than under ideal conditions but still acceptable. The estimated accuracy of the measurement provided by the GNSS receiver can be achieved but it performs worse than the accuracy specified in the receivers datasheet. The specified values in the datasheet expect optimal environment with an open sky condition. This could be the cause for the deviation from the specified accuracies. The deviation from the reference measurement of three centimeters is also a good indicator for the precision of the measurement instrument.

## 6 Summary and Outlook

A measurement instrument for the determination of the alignment of trihedral corner reflectors as well as for the determination of the corner reflector's phase center position is successfully developed. It uses a GNSS receiver for the determination of the position and the azimuth angle of the corner reflector and a two axis inclinometer for the determination of the elevation and the roll angle of the corner reflector. A web interface can be used on a mobile phone in order to comfortably view the alignment angles and the phase center position and to enter information about the reflector such as the reflector id or the site name leading to a more time efficient way for the alignment of corner reflectors. The instrument automatically determines the size of the corner reflector by evaluating the baseline length between the main and the auxiliary antenna. When the size cannot be determined automatically, it must be entered over the web interface. The alignment values can be stored inside an internal database and can be pushed to DLR's database when it is connected by ethernet to DLR's intranet. The process of synchronizing the values with DLR's database has not been implemented so far due to missing specification. The measurement instrument is validated with trihedral corner reflectors. The results of the validation look promising. A precise determination of the alignment below  $0.5^\circ$  which is the initial goal for the instrument can be achieved. For the azimuth angle an uncertainty of  $0.2^\circ$  could be reached which is slightly worse than the accuracy as specified by the used GNSS receiver. For the elevation angle an uncertainty of  $0.25^\circ$  can be reached which is slightly worse than the expected accuracy of the inclinometer in the operating temperature range.

For the phase center position, the three dimensional uncertainty is approximately 0.03 meter which is worse than the initially expected accuracy of about 0.01 meter from specification but still acceptable. The accuracy estimated by the receiver can be achieved. When comparing the measurement to a reference measurement performed by a much more precise GNSS receiver, the deviation from this position is still in the estimated accuracy of the GNSS receiver used in the measurement instrument. In table 12 the specification of the developed measurement instrument is given.

In order to extend on the presented measurement instrument, it needs to be validated with dihedral corner reflectors to use it for the alignment of these type of corner reflectors as well. A concept for the usage of the measurement instrument with the dihedral corner reflector is provided. The reference model for the dihedral corner reflector is implemented which can be used with the optimizer in order to transform the model to the ENU frame. Algorithms for the calculation of the attitude angles and the dihedral corner reflector's phase center position are implemented but not tested. In order to start the validation for the dihedral corner reflectors, fixations for the antennas need to be built and the dimensions of the fixations need to be added to the configuration file in order to attach them to

the dihedral corner reflector. In the web interface, an option for the corner reflector type has already been added to switch between the calculation algorithms for the trihedral and the dihedral corner reflector.

Another improvement for the measurement instrument would be to the ability to add a desired alignment angle in the web interface and the measurement instrument to provide visual and auditive feedback how close the current alignment is to the desired one. Therefore, the web interface and the display can be used for visual indication as well as the speaker installed in the display can be used for auditive feedback. A function for the output of pulses on the display's speaker is already implemented. If the speaker of the display is not loud enough an external speaker can be installed as well.

property	value
azimuth angle	0...360° +/- 0.2° ( $3\sigma$ )
elevation angle	-90...+90 +/- 0.25° ( $3\sigma$ )
position uncertainty (3D)	+/- 0.03 m ( $3\sigma$ )
position reference system	ETRS89/DREF91
communication interfaces	Wi-Fi, ethernet, USB
supply voltage	7.2 V ... 14 V
current consumption	typ. 1.9 A
typical runtime	7.81 hours
operating temperature	-10°C ... 70°C
size housing (l x w x h)	0.25 m x 0.3 m x 0.1 m
weight	$\approx$ 3 kg

Table 12: Specifications of the developed measurement instrument for corner reflector alignment

## References

- [1] P. Berens, “Introduction to Synthetic Aperture Radar (SAR),” Research Institute for High-Frequency Physics and Radar Techniques (FHR), Wachtberg, Germany, Tech. Rep. ADA470686, 2006. [Online]. Available: <https://apps.dtic.mil/sti/pdfs/ADA470686.pdf>
- [2] A. Moreira, P. Prats-Iraola, M. Younis, G. Krieger, I. Hajnsek, and K. P. Papathanassiou, “A tutorial on synthetic aperture radar,” *IEEE Geoscience and Remote Sensing Magazine*, vol. 1, no. 1, pp. 6–43, Mar. 2013. [Online]. Available: <http://ieeexplore.ieee.org/document/6504845/>
- [3] A. Doerry, “Reflectors for SAR performance testing.” Tech. Rep. SAND2008-0396, 929123, Jan. 2008. [Online]. Available: <https://www.osti.gov/servlets/purl/929123/>
- [4] K. Sarabandi and Tsen-Chieh Chiu, “Optimum corner reflectors design,” in *Proceedings of the 1996 IEEE National Radar Conference*. Ann Arbor, MI, USA: IEEE, 1996, pp. 148–153. [Online]. Available: <http://ieeexplore.ieee.org/document/510672/>
- [5] F. J. Lohmar, “World geodetic system 1984 — geodetic reference system of GPS orbits,” in *GPS-Techniques Applied to Geodesy and Surveying*, E. Groten and R. Strauß, Eds. Berlin/Heidelberg: Springer-Verlag, 1988, vol. 19, pp. 476–486, series Title: Lecture Notes in Earth Sciences. [Online]. Available: <http://link.springer.com/10.1007/BFb0011360>
- [6] Y. Lu, *BDS/GPS Dual-Mode Software Receiver: Principles and Implementation Technology*, ser. Navigation: Science and Technology. Singapore: Springer Singapore, 2021, vol. 10. [Online]. Available: <https://link.springer.com/10.1007/978-981-16-1075-2>
- [7] J. Glabe, “Euler Angles and Roll Pitch Yaw Representation,” in *Encyclopedia of Robotics*, M. H. Ang, O. Khatib, and B. Siciliano, Eds. Berlin, Heidelberg: Springer Berlin Heidelberg, 2021, pp. 1–3. [Online]. Available: [http://link.springer.com/10.1007/978-3-642-41610-1\\_129-1](http://link.springer.com/10.1007/978-3-642-41610-1_129-1)
- [8] J. Sanz Subirana, J. M. Juan Zornoza, and M. Hernández-Pajares, *GNSS Data Processing, Vol I: Fundamentals and Algorithms*. Noordwijk: ESA Communications, 2013, oCLC: 922681097.
- [9] L. V. Kuylen, F. Boon, and A. Simsky, “Attitude Determination Methods Used in the PolaRx2 Multi-antenna GPS Receiver,” Institute of Navigation, Long Beach, CA, Tech. Rep., Sep. 2005.

- [10] DLR, “TerraSAR-X - Das deutsche Radar-auge im All,” DLR, Bonn, Missionsbroschüre, 2009. [Online]. Available: [https://www.dlr.de/hr/de/PortalData/32/Resources/dokumente/broschueren/TerraSAR-X\\_web\\_Broschuere2010\\_LoRes.pdf](https://www.dlr.de/hr/de/PortalData/32/Resources/dokumente/broschueren/TerraSAR-X_web_Broschuere2010_LoRes.pdf)
- [11] M. Bartusch, I. Hajnsek, J. Janoth, C. Marschner, D. Miller, A. Moreira, and M. Zink, “TanDEM-X - Die Erde in drei Dimensionen,” DLR, Köln, Missionsbroschüre, 2009. [Online]. Available: [https://www.dlr.de/hr/de/PortalData/32/Resources/dokumente/broschueren/TanDEM-X\\_web\\_Broschuere2010.pdf](https://www.dlr.de/hr/de/PortalData/32/Resources/dokumente/broschueren/TanDEM-X_web_Broschuere2010.pdf)
- [12] DLR, “DLR - Institut für Hochfrequenztechnik und Radarsysteme - Home,” 2022. [Online]. Available: <https://www.dlr.de/hr/de/desktopdefault.aspx>
- [13] —, “DLR - Institut für Hochfrequenztechnik und Radarsysteme - Satelliten-SAR-Systeme,” 2022. [Online]. Available: <https://www.dlr.de/hr/de/desktopdefault.aspx/tabid-2328/>
- [14] R. Bamler, “Principles of Synthetic Aperture Radar,” *Surveys in Geophysics*, vol. 21, no. 2/3, pp. 147–157, 2000. [Online]. Available: <http://link.springer.com/10.1023/A:1006790026612>
- [15] K. Tomiyasu, “Tutorial review of synthetic-aperture radar (SAR) with applications to imaging of the ocean surface,” *Proceedings of the IEEE*, vol. 66, no. 5, pp. 563–583, 1978. [Online]. Available: <http://ieeexplore.ieee.org/document/1455230/>
- [16] E. Lertes, *Funkortung und Funknavigation*, W. Schneider, Ed. Wiesbaden: Vieweg+Teubner Verlag, 1995. [Online]. Available: <http://link.springer.com/10.1007/978-3-663-12124-4>
- [17] Y. Lihai, G. Jialong, J. Kai, and Y. Yanmei, “Research on synthetic aperture radar imaging characteristics of point targets,” in *2009 2nd Asian-Pacific Conference on Synthetic Aperture Radar*. Xian, Shanxi, China: IEEE, Oct. 2009, pp. 282–285. [Online]. Available: <http://ieeexplore.ieee.org/document/5374150/>
- [18] A. Saeed and O. Hellwich, “Design, deployment, and localization of bidirectional corner reflectors for TerraSAR-X,” in *2017 IEEE Microwaves, Radar and Remote Sensing Symposium (MRRS)*. Kiev, Ukraine: IEEE, Aug. 2017, pp. 267–270. [Online]. Available: <http://ieeexplore.ieee.org/document/8075079/>
- [19] Z. Xu, X. Ai, Q. Wu, F. Zhao, and S. Xiao, “Coupling Scattering Characteristic Analysis of Dihedral Corner Reflectors in SAR Images,” *IEEE Access*, vol. 6, pp. 78 918–78 930, 2018. [Online]. Available: <https://ieeexplore.ieee.org/document/8567983/>



- [20] B. Görres, “Vom globalen Bezugssystem bis zur Umsetzung für die Praxis,” in *GNSS 2010 – Vermessung und Navigation im 21. Jahrhundert*, ser. DVW-Schriftenreihe. Augsburg: Wißner-Verlag, 2010, vol. Bd. 63.
- [21] P. Zhang, C. Xu, C. Hu, and Y. Chen, “Coordinate Transformations in Satellite Navigation Systems,” in *Advances in Electronic Engineering, Communication and Management Vol.2*, D. Jin and S. Lin, Eds. Berlin, Heidelberg: Springer Berlin Heidelberg, 2012, vol. 140, pp. 249–257, series Title: Lecture Notes in Electrical Engineering. [Online]. Available: [http://link.springer.com/10.1007/978-3-642-27296-7\\_40](http://link.springer.com/10.1007/978-3-642-27296-7_40)
- [22] J. Zhu, “Conversion of Earth-centered Earth-fixed coordinates to geodetic coordinates,” *IEEE Transactions on Aerospace and Electronic Systems*, vol. 30, no. 3, pp. 957–961, Jul. 1994. [Online]. Available: <http://ieeexplore.ieee.org/document/303772/>
- [23] R. Sun, Q. Cheng, and J. Wang, “Precise vehicle dynamic heading and pitch angle estimation using time-differenced measurements from a single GNSS antenna,” *GPS Solutions*, vol. 24, no. 3, p. 84, Jul. 2020. [Online]. Available: <https://link.springer.com/10.1007/s10291-020-01000-2>
- [24] Septentrio, “mosaic-H Reference Guide,” Septentrio, Leuven, Datasheet, 2022.
- [25] K. Waldron and J. Schmiedeler, “Kinematics,” in *Springer Handbook of Robotics*, B. Siciliano and O. Khatib, Eds. Berlin, Heidelberg: Springer Berlin Heidelberg, 2008, pp. 9–33. [Online]. Available: [http://link.springer.com/10.1007/978-3-540-30301-5\\_2](http://link.springer.com/10.1007/978-3-540-30301-5_2)
- [26] F. Tamjid, F. Foroughian, C. M. Thomas, A. Ghahremani, R. Kazemi, and A. E. Fathy, “Toward High-Performance Wideband GNSS Antennas-Design Tradeoffs and Development of Wideband Feed Network Structure,” *IEEE Transactions on Antennas and Propagation*, vol. 68, no. 8, pp. 5796–5806, Aug. 2020. [Online]. Available: <https://ieeexplore.ieee.org/document/9055417/>
- [27] M. Hoffmann, P. Kryszkiewicz, and G. P. Koudouridis, “Modeling of Real Time Kinematics localization error for use in 5G networks,” *EURASIP Journal on Wireless Communications and Networking*, vol. 2020, no. 1, p. 31, Dec. 2020. [Online]. Available: <https://jwcn-urasipjournals.springeropen.com/articles/10.1186/s13638-020-1641-8>
- [28] P. Jonge and C. Tiberius, “The LAMBDA method for integer ambiguity estimation: implementation aspects,” *Delft Geodetic Computing Centre LGR Series*, vol. 12, Jul. 1998.

- [29] C. Eling, P. Zeimet, and H. Kuhlmann, “Development of an instantaneous GNSS/MEMS attitude determination system,” *GPS Solutions*, vol. 17, no. 1, pp. 129–138, Jan. 2013. [Online]. Available: <http://link.springer.com/10.1007/s10291-012-0266-8>
- [30] X. Wang, Y. Yao, C. Xu, Y. Zhao, and H. Zhang, “An Improved Single-Epoch Attitude Determination Method for Low-Cost Single-Frequency GNSS Receivers,” *Remote Sensing*, vol. 13, no. 14, p. 2746, Jul. 2021. [Online]. Available: <https://www.mdpi.com/2072-4292/13/14/2746>
- [31] Septentrio, “Septentrio mosaic-go heading,” Leuven, Datasheet, 2022. [Online]. Available: <https://septentrio.sharepoint.com/Marketing4Sales/Shared%20Documents/Forms/AllItems.aspx?id=%2FMarketing4Sales%2FShared%20Documents%2FDatasheets%2Fmosaic%2Fmosaic%2Dgo%20heading%2FSeptentrio%5Fmosaic%5Fgo%5Fheading%5FLR%2Epdf&parent=%2FMarketing4Sales%2FShared%20Documents%2FDatasheets%2Fmosaic%2Fmosaic%2Dgo%20heading&p=true&ga=1>
- [32] T. Connectivity, “AXISENSE-2 SERIES USB TILT SENSOR,” TE Connectivity LTD, Datasheet, 2020. [Online]. Available: [https://www.te.com/commerce/DocumentDelivery/DDEController?Action=showdoc&DocId=Data+Sheet%7FTES\\_DS\\_AXISENSE-2\\_USB-90%7FA3%7Fpdf%7FEnglish%7FENG\\_DS\\_TES\\_DS\\_AXISENSE-2\\_USB-90\\_A3.pdf%7FG-NSDOG2-021](https://www.te.com/commerce/DocumentDelivery/DDEController?Action=showdoc&DocId=Data+Sheet%7FTES_DS_AXISENSE-2_USB-90%7FA3%7Fpdf%7FEnglish%7FENG_DS_TES_DS_AXISENSE-2_USB-90_A3.pdf%7FG-NSDOG2-021)
- [33] Tallysman, “TW7972 Triple-band GNSS Antenna + L-band,” Tallysman Inc., Datasheet, 2019. [Online]. Available: <https://www.tallysman.com/app/uploads/2018/05/Tallysman%C2%AE-TW7972-Datasheet.pdf>
- [34] E. Assembly, “EA PLUG-Serie,” Electroinc Assembly, Gilching, Datasheet, 2019.
- [35] Leica, “Leica Viva GS16,” Leica Geosystems, Heerbrugg, Swiss, Datasheet, 2022.
- [36] B. R. Johnson, E. Cabuz, H. B. French, and R. Supino, “Development of a MEMS gyroscope for northfinding applications,” in *IEEE/ION Position, Location and Navigation Symposium*. Indian Wells, CA, USA: IEEE, May 2010, pp. 168–170. [Online]. Available: <http://ieeexplore.ieee.org/document/5507133/>
- [37] B. P. Dyches, “What is the North Star and How Do You Find It?” 2021. [Online]. Available: <https://solarsystem.nasa.gov/news/1944/what-is-the-north-star-and-how-do-you-find-it>
- [38] Leica, “Leica TS16 Datenblatt,” Leica Geosystems, Heerbrugg, Swiss, Datasheet, 2020.

- [39] SciPy, “`scipy.optimize.least_squares` — SciPy v1.10.0 Manual,” 2023. [Online]. Available: [https://docs.scipy.org/doc/scipy/reference/generated/scipy.optimize.least\\_squares.html](https://docs.scipy.org/doc/scipy/reference/generated/scipy.optimize.least_squares.html)

## A Appendix

### A.1 Software Modules Flow Charts

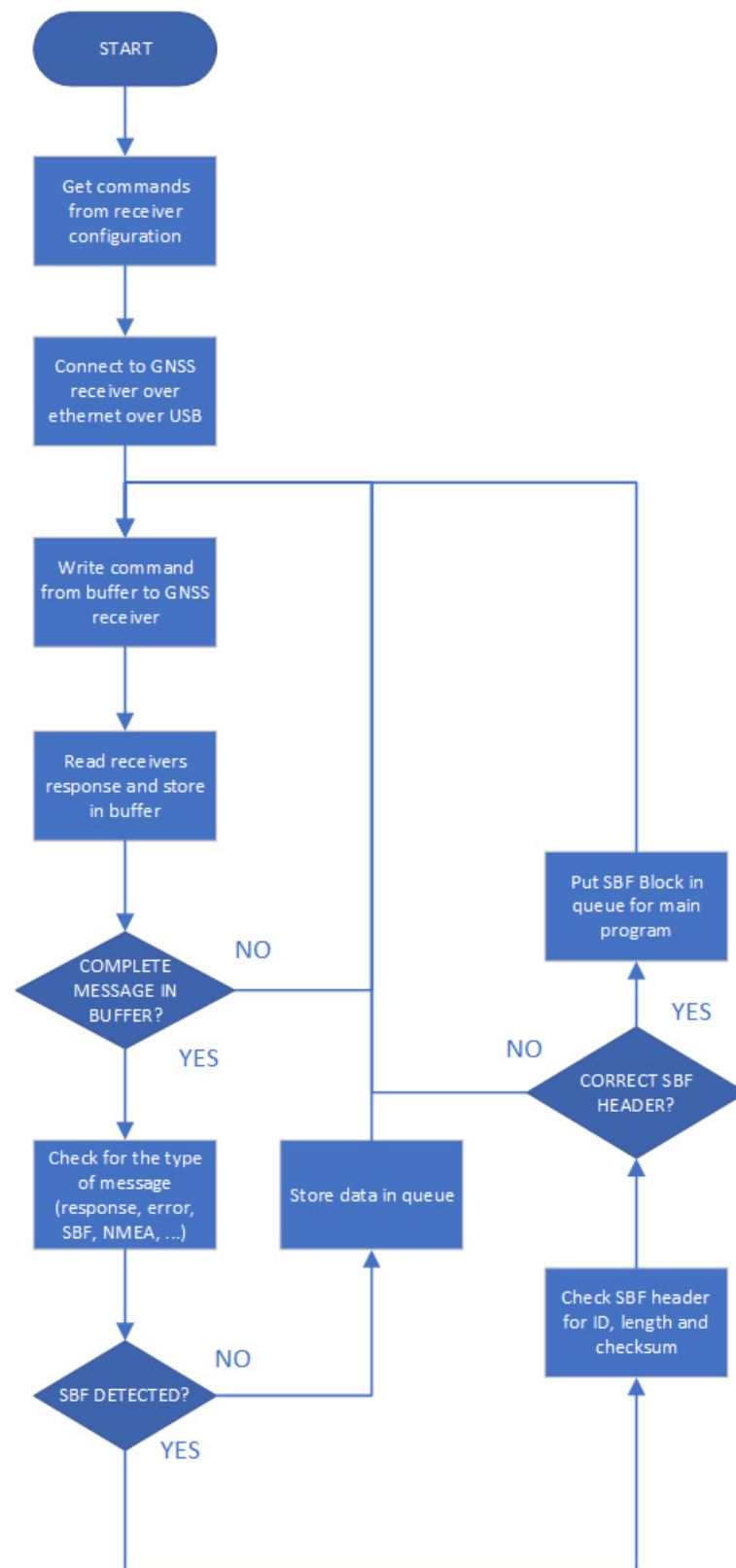


Figure 25: Flow chart of the receiver interface process

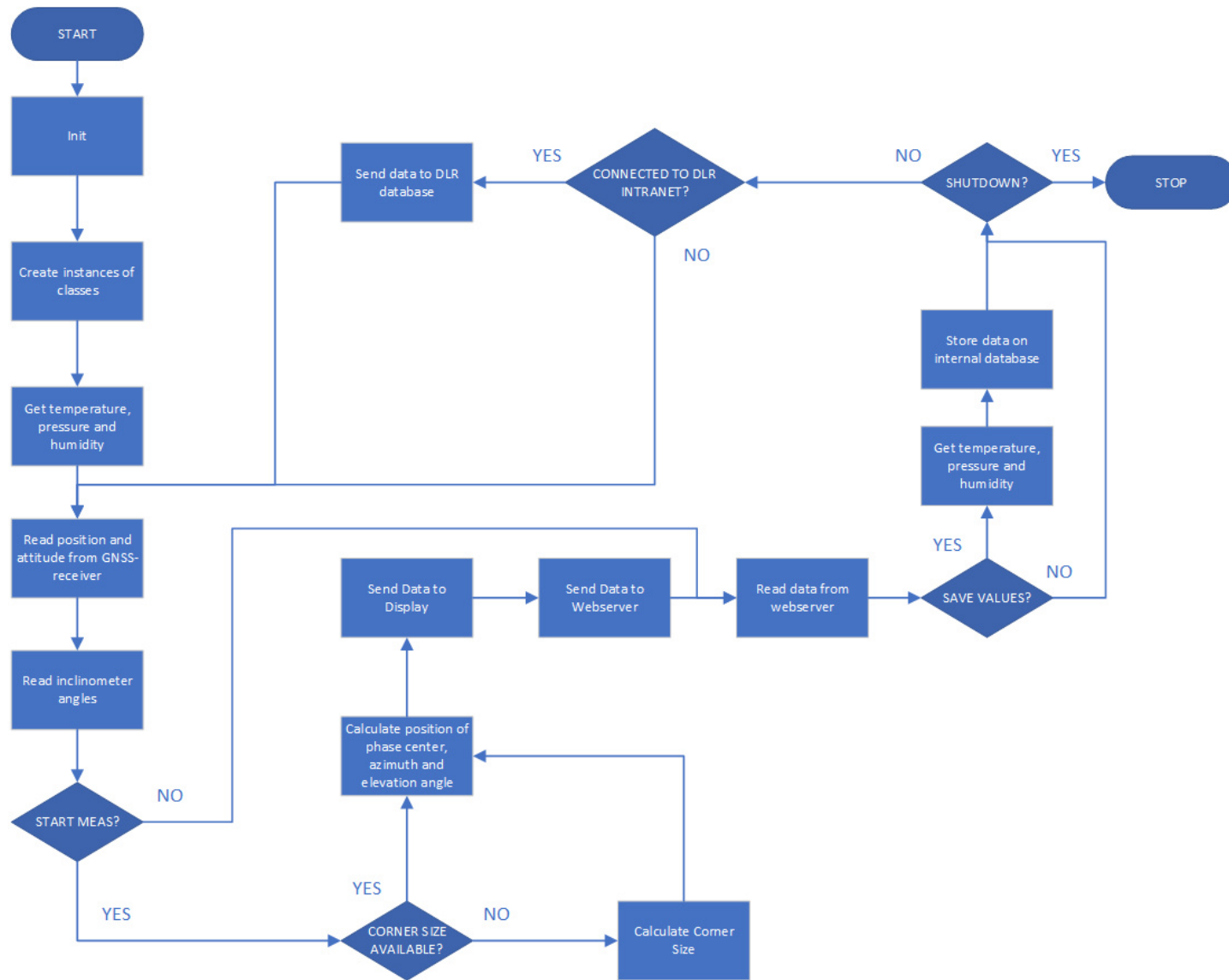


Figure 26: Flow chart of the main program